Acta Materialia 304 (2026) 121818

Contents lists available at ScienceDirect

Acta Materialia

journal homepage: www.elsevier.com/locate/actamat

Computation of displacements from strain fields: Derivation, validation, and application

Abdalrhaman Koko [a,b,*], Elsiddig Elmukashfi [c], Phani S. Karamched [a], T. James Marrow [a]

[a] Department of Materials, University of Oxford, Oxford OX1 3PH, United Kingdom
[b] National Physical Laboratory, Hampton Road, Teddington TW11 0LW, United Kingdom
[c] School of Engineering, University of Leicester, Leicester LE17RH, United Kingdom

ARTICLE INFO

Keywords:
Strain integration
Displacement reconstruction
HR-EBSD
Finite element method
Crack-tip fields
Stress intensity factors
J-integral
Diffraction-based strain mapping
Microscale fracture mechanics

ABSTRACT

High-resolution experimental methods now yield detailed elastic strain fields around cracks and other stress concentrators; however, these measurements alone cannot provide the displacement gradients required for a quantitative fracture assessment. Existing approaches to recover displacement fields from such data are either restricted to two dimensions, rely on strong assumptions about material behaviour, or lack robustness when confronted with noise typical of diffraction-based strain mapping. To address this limitation, we have developed a finite-element framework that reconstructs continuous displacement fields directly from measured deformation gradients without prescribing external loads or boundary conditions. The approach formulates strain integration as an over-determined least-squares problem defined on linear or quadratic elements in two and three dimensions. Validation using analytical 2D mode-I and 3D mixed-mode crack-tip fields demonstrates that the recovered displacements and derived stress intensity factors deviate from theoretical values by <4 %. The method is further applied to HR-EBSD measurements around Vickers-indentation cracks in monocrystalline silicon, where the reconstructed fields reproduce AFM-measured surface topography and reveal distinct residual mixed-mode loading at neighbouring cracks. These results show that full-field diffraction-based strain measurements can be converted into mechanically meaningful displacement and fracture parameters with high fidelity. The method provides a practical route for quantifying crack driving forces in complex microstructures and can be extended to three-dimensional diffraction techniques and in situ studies of evolving damage.

1. Introduction

Understanding material fracture is critically important across multiple length scales – from the microscopic processes inside materials to the macroscopic behaviour of entire structures. Fracture phenomena span a vast range of scales, occurring in contexts as mundane as everyday tool breakage and as colossal as geological faults [1,2]. To study deformation and fracture experimentally across these scales, researchers rely on methods that measure the full-field deformation or strain. In recent decades, various non-contact techniques have been developed to map strain distributions with high spatial resolution. Major techniques for measuring strain fields at different scales include 2D digital image correlation (DIC) [3–6] and 3D digital volume correlation (DVC) [7–9]. These are widely used methods that can determine the displacement field by precisely tracking the movement of features (speckle patterns) between 2D or 3D images taken before and after deformation by optical, electron and X-ray microscopy.

On the other hand, diffraction-based techniques can measure and map elastic strain fields in materials by measuring the changes in the crystal lattice spacing. Over the past decade, advanced characterisation techniques – such as high-angular-resolution electron backscatter diffraction (HR-EBSD) [10–14], convergent beam electron diffraction (CBED) [15], and Bragg coherent diffraction imaging (BCDI) – have enabled high-fidelity measurement of elastic strains at micro- and nanoscales. Similar progress has been made using transmission electron microscopy (TEM) methods, nano-beam electron diffraction (NBED) [16], high-resolution TEM [17], and dark-field electron holography (DFEH) [18], offering nanometre-scale spatial resolution with high strain sensitivity. Synchrotron X-ray techniques, such as high-energy diffraction microscopy [19,20], diffraction contrast tomography [21], and 3D Laue microdiffraction [22–24], have extended these measurements to three dimensions with comparable strain resolution [19,25,

* Corresponding author.
E-mail address: abdo.koko@material.ox.ac.uk (A. Koko).

https://doi.org/10.1016/j.actamat.2025.121818
Received 24 October 2025; Received in revised form 27 November 2025; Accepted 8 December 2025
Available online 9 December 2025

26]. Neutron diffraction can similarly be applied for strain measurement in materials [27,28]. Given its low absorption, neutron diffraction allows for the analysis of large bulk samples at the engineering scale [29].

These advanced experimental methods now allow researchers to visualise how strain is distributed around stress localisations, including crack tips, across different specimen sizes and types of materials, and thus evaluate fracture metrics. One such is the *J*-integral – a path-independent integral used to characterise the thermodynamic crack driving force – that is defined (in one common form) as an encirclement of the crack tip [30–32]:

$$J = \oint_{\Gamma} \left(W n_x - \sigma_{ij} \frac{\partial u_i}{\partial x} n_j \right) ds \tag{1}$$

where W is the strain energy density, n is the normal to the integration path Γ, ds is the length increment along the integration path, and u_i are displacement components.

In mode I terms, one of the key contributions involves the gradient of the crack-opening displacement (vertical displacement u_y) in the crack propagation direction (x). Specifically, the term $\partial u_y/\partial x$ (sometimes denoted $u_{2,1}$ in tensor notation) appears in the integrand. However, strain-field measurements do not directly yield this quantity. The transverse displacement gradient term $\partial u_y/\partial x$ is only one part of the shear strain ε_{xy}, which also contains the lateral gradient $\partial u_x/\partial y$. In other words, a given field of measured strains, i.e., $\varepsilon_{xx},\ \varepsilon_{yy},\ \varepsilon_{xy}$ in 2D and additional $\varepsilon_{xz},\ \varepsilon_{yz}, \varepsilon_{zz}$ in 3D is insufficient to uniquely determine the individual displacement derivatives needed in the formulation of the *J*-integral. All other terms in the *J* calculation (e.g. W or σ_{ij}) can be obtained from constitutive properties (i.e., elastic moduli) or directly from measured strains; however, this particular component of the displacement field is missing as it is not measured directly.

In light of this issue, an important step is required before full-field experimental data can be used for fracture mechanics calculations: integrating the measured strain field to recover the displacement field. One can obtain the actual displacement components across the field by performing strain integration (essentially solving the inverse of the differentiation that yields strain from displacement). With the reconstructed displacement field, fracture parameters can then be evaluated – for instance, by inserting u_i into contour integrals for J [8,33,34], or by fitting the near-tip u-field to analytical crack solutions to extract K-values [7,35,36]. This integration process is non-trivial because experimental strain data may contain noise and may not exactly satisfy continuum compatibility conditions. Nonetheless, developing robust techniques to derive $u(x,y)$ from $\varepsilon_{ij}(x,y)$ is the central challenge we address. Thus, the central challenge is developing a robust, scale-independent method for integrating high-resolution strain measurements into accurate displacement fields, even in non-uniform microstructures and steep gradients.

In this paper, we provide a novel solution for this hurdle using a method that employs the finite element method to integrate the strain field by discretising a domain of interest. A system of equations is then assembled and solved for the nodal displacements using a least squares method. Initially, we validate the method by studying the two-dimensional and three-dimensional crack tip deformation fields under pure mode I and mixed mode loading, respectively, for a linear elastic material. Subsequently, we investigate the full strain field around cleavage cracks propagating from a Vickers indentation, using HR-EBSD to determine the residual stress intensity factors acting on cracks initiated by the indentation.

2. Numerical method

Consider a class of problems where the deformation field is provided through measurements such as the engineering strain or the deformation gradient in the current configuration. The proposed formulation aims to determine the displacement field by integrating the deformation measures at specified points (i.e., mesh nodes). Thus, we consider a body subjected to mechanical loading that results in deformation defined by the deformation gradient.

$$F_{ij} = \frac{\partial x_i}{\partial X_j} = \delta_{ij} + \frac{\partial u_i}{\partial X_j} \tag{2}$$

where $X_i,\ x_i,\ 1,2,3,$ is a standard Cartesian coordinate system for the reference and deformed configurations, respectively, $u_i = x_i - X_i$ is the displacement vector, δ_{ij} is the second-order identity tensor and $H_{ij} = \partial u_i/\partial X_j$ is the displacement gradient. The displacement gradient can be split into an infinitesimal strain ε_{ij} (symmetric part) and rotations ω_{ij} (asymmetric part) as:

$$H_{ij} = \varepsilon_{ij} + \omega_{ij}, \tag{3}$$

with

$$\varepsilon_{ij} = \frac{1}{2}\left(\frac{\partial u_i}{\partial X_j} + \frac{\partial u_j}{\partial X_i}\right),\ \ \omega_{ij} = \frac{1}{2}\left(\frac{\partial u_i}{\partial X_j} - \frac{\partial u_j}{\partial X_i}\right). \tag{4}$$

The body can be discretised using finite elements to determine the nodal displacement field. Thus, the displacement field is interpolated as:

$$u_i(X_j,t) = \sum_{I=1}^{N_{\text{nodes}}} N_I(X_j) u_{iI}(t) \tag{5}$$

where N_I are the standard finite element shape functions, which can also be expressed in terms of the parent element coordinates $\xi_i \in (\xi,\eta,\zeta)$, N_{nodes} is the total number of nodes in the mesh and u_{iI} are the values of the nodal displacements. The reference and current configurations are respectively interpolated as:

$$X_i(X_j,t) = \sum_{I=1}^{N_{\text{nodes}}} N_I(\xi_j) X_{iI},\ \ x_i(X_j,t) = \sum_{I=1}^{N_{\text{nodes}}} N_I(\xi_j) x_{iI}(t), \tag{6}$$

where X_{iI} and x_{iI} are the coordinates of node $I \in \Omega$ in the reference and current configurations, respectively. Using the definitions in Eqs. (3) and (5), the displacement gradient can be obtained by:

$$H_{ij}(X_k,t) = \frac{\partial u_i(X_k,t)}{\partial X_j} = \sum_{I=1}^{N_{\text{nodes}}} \frac{\partial N_I(\xi_k)}{\partial X_j} u_{iI}(t) = \sum_{I=1}^{N_{\text{nodes}}} \frac{\partial N_I}{\partial \xi_l} \underbrace{\frac{\partial \xi_l}{\partial X_j}}_{J_{jl}^{-1}} u_{iI}(t), \tag{7}$$

where $J_{ij} = \partial X_i/\partial \xi_j$ is the mapping gradient from the reference configuration to the parent domain, which can be calculated using Eq. (8):

$$J_{ij} = \frac{\partial X_i}{\partial \xi_j} = \sum_{I=1}^{N_{\text{nodes}}} \frac{\partial N_I}{\partial \xi_j} X_{iI}. \tag{8}$$

The mapping gradient of the current configuration to the parent domain is similarly determined from Eq. (9):

$$j_{ij} = \frac{\partial x_i}{\partial \xi_j} = \sum_{I=1}^{N_{\text{nodes}}} \frac{\partial N_I}{\partial \xi_j} x_{iI}, \tag{9}$$

where $F_{ij} = j_{ik} J_{kj}^{-1}$. Hence, the displacement gradient can be written in terms of the current configuration as follows:

$$H_{ij}(x_k,t) = \sum_{I=1}^{N_{\text{nodes}}} \frac{\partial N_I}{\partial \xi_l} \frac{\partial \xi_l}{\partial x_m} \frac{\partial x_m}{\partial X_j} u_{iI}(t) = \sum_{I=1}^{N_{\text{nodes}}} \frac{\partial N_I}{\partial \xi_l} j_{lm}^{-1} F_{mj}\, u_{iI}(t) \tag{10}$$

Thus, Eqs. (7) and (10) provide an expression for the displacement gradient at any point in the reference and current configurations, X_k and x_k, respectively, within the element at a given instant of time t. It should be noted that the displacement interpolation in Eq. (5) requires that the shape functions exist and be continuous, satisfying C_0 continuity. This results in a constant displacement gradient within the element, which can be discontinuous across elements. Using higher-order shape functions (ensuring C_1 continuity or higher) guarantees the continuity of both displacement and its gradient.

Consider experimental measurements of the deformation gradient $\overline{F}_{ij}$ in a domain of interest at given points $\overline{x}_k$ in the current or intermediate configuration. The experiment can be conducted in situ or ex situ, where the current or intermediate configuration represents the deformed configuration, respectively. The displacement gradient $\overline{H}_{ij}$ is determined from Eq. (7). The domain of interest is discretised using the total number of elements N_{Ele} and the total number of nodes N_{nodes}. A set of computational points N_{P}, which lie within the element, can be chosen such that the total number of measurement points is $N_{CP} = N_{\text{Ele}} \times N_{\text{P}}$. The position of the computational points is determined by uniform measurement steps, which are equal in all directions, as is common in most experimental methods. Consequently, the discretisation can be designed so that each element type contains a certain number of computational points. This may result in some nodal and computational points overlapping. In such cases, the continuity of the displacement gradient is not ensured at the nodes. However, selecting computation points within the element's interior always ensures the continuity of the displacement gradient. Additionally, from the interpolation requirements, the minimum number of computation points is $N_P = n - 1$, where n is the degree of the polynomial of the shape functions.

Therefore, Eq. (10) can be used to express the displacement gradient at the measurement points in terms of the nodal displacements. This leads to a system of equations where the unknowns are the nodal displacements u_{iI}, with the displacement gradient, the deformation gradient on the left-hand side, and the deformation gradient on the right-hand side prescribed from the experimental measurements. The total number of unknowns is $N_{\text{Un}} = N_{\text{nodes}} \times N_{\text{Dim}}$, where N_{Dim} is the number of dimensions of the problem, and the total number of equations becomes $N_{\text{Eq}} = N_{\text{Ele}} \times N_{\text{P}} \times N_{\text{d}}$, where N_{d} is the number of components of the deformation measure (i.e., in 2D problems is $N_{\text{d}} = 4$ and in 3D problems is $N_{\text{d}} = 9$). The system of equations can be written in the algebraic form:

$$A_{ij} d_j = b_i, \tag{11}$$

where A_{ij} is a N_{Eq} x N_{Un} coefficients matrix that depends on the deformation gradient $\overline{F}_{ij}$, d_j is a vector that encapsulates the unknown nodal displacements u_{iI}, b_i is a vector that encapsulates the displacement gradient from the measurements $\overline{H}_{ij}$. The details of these operators are provided in the Supplementary Information. The linear algebraic equations in (11) result in one of three solution sets [37]:

(i) If $N_{\text{Eq}} = N_{\text{Un}}$, A_{ij} has a full rank, and its inverse A_{ij}^{-1} is unique. Thus, this will lead to a single unique solution as

$$d_j = A_{ij}^{-1} b_i. \tag{12}$$

(ii) If $N_{\text{Eq}} > N_{\text{Un}}$, the system of equations is *overdetermined*, and the solution can be best solved using an optimisation method such as the least-squares method. Thus, a minimisation of the square error can be written as below:

$$\min \| A_{ij} d_j - b_i \|^2 \tag{13}$$

The solution to the minimisation problem of the values of the nodal displacements d_j is then obtained by Eq. (14).

$$d_j = \left(A_{ij}^T A_{ij} \right)^{-1} A_{ij}^T b_i \tag{14}$$

(iii) If $N_{\text{Eq}} < N_{\text{Un}}$, the system of equations is *underdetermined* with an infinite number of solutions unless the problem is subjected to a constraint or regularisations (e.g., condition matrix when using the pseudoinverse method ($\text{cond}(A_{ij}) = \| A_{ij} \| \| A_{ij}^{+} \|$, where A_{ij}^{+} is the Moore–Penrose inverse of an A_{ij} matrix).

A unique solution can be obtained when the system of equations is of full rank. An overdetermined system of equations will still have a solution if some equations are linear combinations of others. Conversely, a non-unique solution may arise from an underdetermined system of equations. Therefore, the discretisation can be designed by selecting an appropriate number of computation points per element and the appropriate interpolation function to ensure a unique solution. The implementation details, including the shape functions for linear and quadratic elements, as well as their coefficient matrices and right-hand-side vectors, are provided in the Supplementary materials.

It should be emphasised that the integration does not impose any external boundary conditions or applied loads. The recovered displacement field is the one that is most consistent with the measured elastic strains, regardless of whether those strains originate from residual stress, external constraint, or local incompatibility. Because the system is overdetermined, the solution is stabilised by the interior measurements rather than by points near boundaries, and local discontinuities (for example, along crack flanks) do not propagate unless they dominate the region. Rigid-body offsets and rotations, which are not encoded in strain, are removed after integration as described later in Section 3.3.4. This makes the method suitable for residual indentation fields and for situations where conventional boundary conditions are unknown or cannot be specified. However, caution needs to be exercised when integrating polycrystals and macro-cracks due to the errors from pattern overlap near grain boundaries [38] and noise near discontinuities [39].

Additionally, note that diffraction-based strain mapping techniques, including HR-EBSD, provide only the elastic strain tensor; plastic strain and other inelastic components are not measurable directly. The present formulation is therefore correctly limited to linear elasticity, since the integrated displacement field must be compatible with the measured elastic lattice distortion. The method does not assume material isotropy, as anisotropy is accounted for only through the constitutive law when stresses or fracture parameters are computed. Extending the approach to nonlinear materials would require experimental access to the total deformation gradient, which is not available in diffraction techniques and lies outside the scope of this work.

3. Illustrative examples

The methods used are detailed in the following sections. The numerical method for approximating the displacement from the measured strain or deformation gradient field is derived. This method is then applied to a measured HR-EBSD field around a Vickers indent impression in a monocrystalline silicon sample, as discussed in the experimental part of the methodology (Section 3.3).

3.1. Synthetic 2D mode I crack tip field

Firstly, a theoretical strain field will be used to predict the displacement field using the proposed method as implemented in MATLAB using the Object-Oriented method (i.e., FE-OOM) with a detailed comparison between the expected field, the only other method reported in the literature (JMAN_S [40]), and the actual displacement field to show the accuracy of the solution. In JMAN_S, the measured in-plane elastic strain field is discretised with a measurement point centred inside a square linear element with four nodes. The measurement point becomes the Gauss point, as illustrated for each element. The elastic field is then integrated into displacement using the finite difference method. Solving the equations uses the Trust-Region-Reflective least squares algorithm [41], which is natively implemented in MATLAB, utilising the Cholesky factorisation method. The method works for full matrices with a regularised grid. For more details, refer to [42].

3.1.1. Analytical dataset

We consider a 2D problem of a crack in an infinite elastic body subjected to pure mode I and mixed-mode conditions. The 2D asymptotic solution of the crack tip stress field for a linear elastic material is given by the Westergaard solution [43]. The strain field can be derived from the crack tip stress using Hooke's law for isotropic elastic materials as follows:

$$\varepsilon_{ij} = \frac{1}{2\mu\sqrt{2\pi r}}\left[K_I f_{ij}^{(I)}(\theta,\chi) + K_{II} f_{ij}^{(II)}(\theta,\chi) + K_{III} f_{ij}^{(III)}(\theta,\chi)\right] + O\left(r^{\frac{1}{2}}\right),$$

$$\varepsilon_{yy} = \frac{1}{2\mu}\frac{K_I}{\sqrt{2\pi r}}\cos\left(\frac{\theta}{2}\right)\left[\chi + \sin\left(\frac{\theta}{2}\right)\sin\left(\frac{3\theta}{2}\right)\right].$$

$$\varepsilon_{xy} = \frac{1}{2\mu}\frac{K_I}{\sqrt{2\pi r}}\cos\left(\frac{\theta}{2}\right)\left[\chi + \sin\left(\frac{\theta}{2}\right)\sin\left(\frac{3\theta}{2}\right)\right]. \tag{15}$$

where (x, y) and (r, θ) are the Cartesian and polar coordinates of coordinate systems, respectively, that are centred at the crack tip, K_I is mode I stress intensity factor, $\mu = E/2(1+\nu)$ is the shear modulus, E is Young's modulus, ν is Poisson's ratio and $\chi = (1-\nu)/(1+\nu)$ for plane stress and $\chi = 1 - 2\nu$ for plane strain. Using Eq. (15) and the definition of the strain components, the displacement in x and y-directions, u_x and u_y, can be expressed by

$$u_x = \frac{K_I}{2\mu}\sqrt{\frac{r}{2\pi}}\cos\left(\frac{\theta}{2}\right)\left[k - 1 + 2\sin^2\left(\frac{\theta}{2}\right)\right],$$

$$u_y = \frac{K_I}{2\mu}\sqrt{\frac{r}{2\pi}}\sin\left(\frac{\theta}{2}\right)\left[k + 1 + 2\cos^2\left(\frac{\theta}{2}\right)\right] \tag{16}$$

where the parameter $\kappa = 3 - 4\nu$ for plane stress and $\kappa = (3-\nu)/(1+\nu)$ for plane strain. The choice of crack field is due to the severity of the deformation and the large deformation gradient near the crack tip. The approach involves using the analytical strain field to determine the displacement field via the numerical method, and then comparing the numerical results with the analytical solution. Thus, to examine the method's validity, we have developed a numerical method; the theoretical strain field in Eq. (15) will be integrated into the displacement field and compared to the theoretical field computed from Eq. (16).

A 2D square domain of $L \times L$ size was considered with the crack parallel to x-axis and its tip is located at the centre of the domain (i.e., $a = L/2$). The strain and displacement components in x and y-directions are determined for a domain of $L = 8$ mm and a mode I stress intensity factor of $K_\mathrm{I} = 30$ MPa·m$^{1/2}$ under plane stress conditions. The isotropic elastic modulus and Poisson's ratio were taken to be $E = 210$ GPa and $\nu = 0.3$, respectively, similar to a ferritic steel. The domain is discretised using a uniform square mesh of element length $l_e = 0.2$ mm (i.e., total of 1331 elements). In the discretisation, linear interpolation functions are adopted, i.e., a 4-node linear element. The number of computational points is taken to be *one* at the centre of the element, as shown in Fig. 1.

3.1.2. Results and discussion

The synthetic strain field was applied to the JMAN_S method, as well as the method developed in this article, which was implemented in MATLAB using object-oriented coding of the finite element method (FE-OOM). FE-OOM used only one Gauss point to allow for comparison. The displacement field in the y-direction, U_y, from both methods and the original field are presented in Fig. 2, a.1–3. The variation between the integrated and original fields around a boundary can be spotted along the crack edge. A boundary in a deformed material creates a

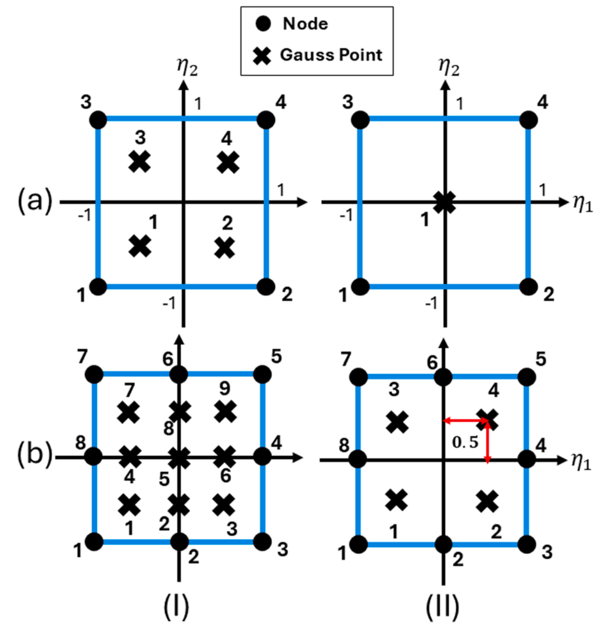

Fig. 1. Schematic of (a) Linear and (b) Quadratic elements with a range of Gauss integration points used for (I) full or (II) reduced integration. A dimensionless local natural coordinate system (η_1, η_2) was defined by its origin at the rectangular element's centre.

discontinuity in the field, accompanied by incompatibility in the deformation field across the boundary. However, FE-OOM shows better accommodation for the incompatibility, which extends across two elements, than JMAN_S, which extends to three pixels. Results from FE-OOM can be improved by increasing the number of integration points (i.e., Gauss points), which cannot be done in JMAN_S.

Also, the shape of the field behaviour ahead of the crack-tip remains curved and consistent between FE-OOM and the original field, contrary to the JMAN_S field. A line profile was taken across the field to compare the actual integrated value to the original, shown in Figure 2a.I with white dotted lines. The results in Fig. 2b show that the proposed method (FE-OOM) accurately predicts the displacement field with a small error value, i.e., ≈ 0.1%, compared to the more significant errors of the JMAN_S method [40]. This is because JMAN_S consider the problem as a finite difference (integration) problem that has a linear form (does not solve for higher-order polynomials), and it uses an optimal weighted sum implemented by the '*lsqlin*' function, a native MATLAB Trust-Region-Reflective Linear Least Squares Algorithm [41], to solve for the nodal displacement. The function achieves global convergence by iterating over a formulated 2D trust-region sub-problem, which adjusts in size – using an overall merit function – until an adequate solution is found within the allowed error range, prioritising efficiency/speed over accuracy. Additionally, JMAN_S assumes that the material is linearly elastic; therefore, compatibility conditions are used to solve for displacement from the linear elastic deformation field of the material. This inhibits JMAN_S from analysing most engineering materials (e.g., elastic-plastic or anisotropic-elastic).

Regardless of the accuracy of the solution obtained with the finite element method, it is only an approximation to the exact solution. Hence, the accuracy of this method was assessed by running the previous analysis but with different element sizes and integrating using a different number of Gaussian points to show their effect on computational time and solution accuracy (δ) using an Intel® Xeon® Gold 6130 CPU fitted with dual 2.10 GHz processors, 512 GB RAM, a 64-bit operating system and x64-based processor, but only used half (32) of the nodes. The solution accuracy (δ) is defined as in Eq. (17), where n is the total number of elements, a_i^W is the value of the ith element obtained directly from the Westergaard solution U_y displcement field and S is for

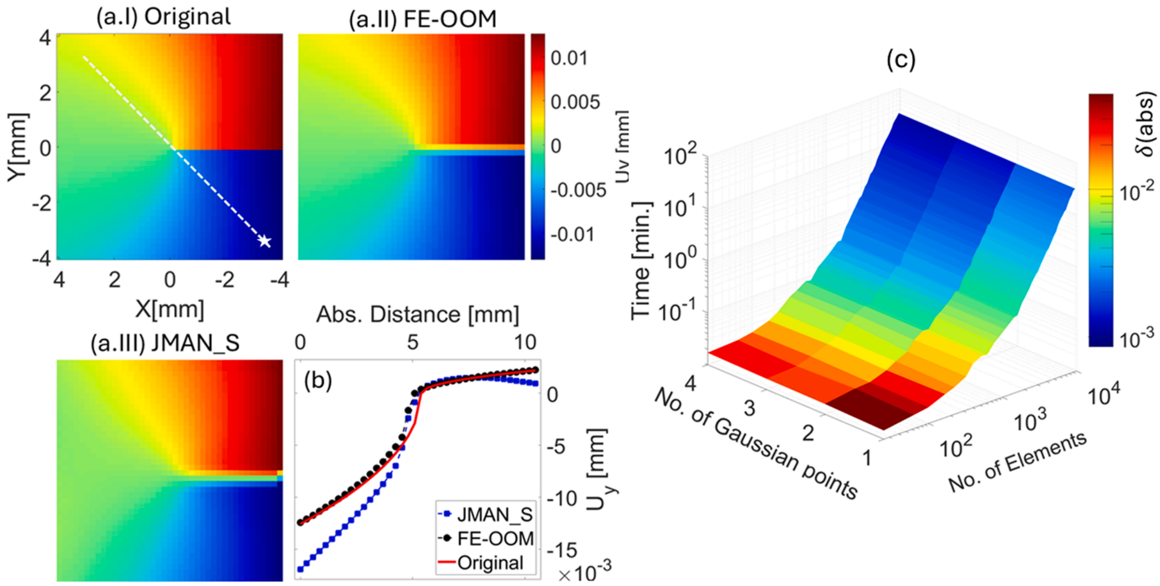

Fig. 2. (a.I) An original $\boldsymbol{U_y}$ displacement field was created using the Westergaard solution, and the integrated field was obtained using (a.II) the finite element object-oriented method (FE-OOM) and (a.III) JMAN_S. (b) A diagonal line profile (along the white dotted line in a.I) was obtained from a.I-III. (c) The computational time and accuracy of solving for nodal displacement using different elements with different integration points using Intel® Xeon® Gold 6130 CPU.

the integrated U_y displacement field.

$$\delta = \frac{1}{n}\sum_{i=1}^{n}\left|\frac{a_i^W - a_i^S}{a_i^W}\right| \tag{17}$$

The computational time and accuracy using different resolutions (i.e., elements in the 8 × 8 mm^2 map) and Gauss points were then plotted in Fig. 2c. Here, the strain measurement point was centred inside an element and then interpolated to the Gauss point(s). From this computational experiment, it can be concluded that the number of Gauss points has a substantial impact on accuracy while having a minimal impact on computational time. In contrast, when only using 1 Gauss point, a steep and gradual increase in accuracy with element quantity can also be observed. This is because, generally, Gauss quadrature integration using high-order terms, i.e., Gaussian points, yields more accurate values with a higher number of orders, thereby improving the integration solution accuracy. Additionally, it yields exact values for polynomials of degree up to 2n-1, where n is the number of quadrature points [44]. However, as highlighted in Fig. 2c, this also increases the computational time. The relationship between the number of elements (N_{el}), number of Gauss points (N_g) and accuracy (δ) can be estimated from Fig. 2c as in Eq. (18) with $R^2 = 0.93$.

$$\delta = \frac{0.2}{\sqrt{N_{el} * N_g}} \tag{18}$$

This implementation allows various methods to ensure efficient and accurate problem computation. The difference between the two types of element order is emphasised. The two-dimensional implementation enables the use of a linear, lower-order element (Fig. 1a) and a quadratic, higher-order element (Fig. 1b), linked to appropriate linear and nonlinear shape functions and Jacobians for full and reduced integration. As the name suggests, the linear element, i.e., $f(x) = ax + b$, is more suitable and efficient for linear integration between two points and does not capture curvature (e.g., quadratic function). Higher-order elements, e.g., $f(x) = ax^2 + bx + c$. On the other hand, they are accurate for higher-order polynomial integration but are far more expensive. Cubic elements, i.e., $f(x) = ax^3 + bx^2 + cx + d$, were not implemented.

When implementing the quadratic element, one faces a problem: for full integration using a quadratic element, nine Gauss points are required, which means the element needs to encompass nine measurement points, compared to four for full integration using a linear element. Then, looking at Fig. 1b, the reader will notice that placing the measurement points where the Gauss points are can be easy when considering a uniform spacing. Nevertheless, the problem arises when the integration for nodal displacement is completed because there is no integration for the centric point. Thus, the integrated map will have a missing point for each element constructed around nine measurement points. Of course, the reverse approach can be taken by placing the measurement point at the element's centre and then linearly interpolating to the Gauss points before (octically[1], 8th-degree polynomial) interpolating the displacement for the centric points from the values of the integrated eight-node displacement surrounding the point. However, interpolating to enrich the map will negate the need to use high-order elements to achieve similar accuracy (similar to segmenting a curve into small lines). Another approach uses reduced quadratic element integration, using nine measurement points, i.e., the 4-point numbered 1 to 4 in Fig. 1bII are 1, 3, 9, and 7 from Fig. 1bI. This leads to reduced accuracy compared to full integration. Note that “full integration” here refers to the order (number of Gauss points) that is required to get an exact solution for an undistorted (or regular shape) element, which has straight edges that meet at edge nodes [45].

This relationship between element order (p) and the number of elements (h), where the accuracy between different element orders converges at a higher number of elements, is not unique to our method but something that was explored by Babuška and Szabó [46] in the hp-adaptive finite element method, which can efficiently solve similar problems. Considering the issue at hand and the number of points in most measured elastic strain fields; linear elements should be enough to approximate the problem accurately with careful consideration given to the number of Gauss points, especially in three-dimensional analysis where full integration is highly recommended as it will at least provide a (tri-) quadratic solution for 3 × 3 × 3 gaussian (points) integration.

3.2. Synthetic 3D mixed-mode crack field

Having searched the existing literature, we did not find a method to

[1] James Cockle proposed the name in 1851 [160]

integrate the three-dimensional (volumetric) strain field into the displacement field. Such data can be obtained using micro-Laue microdiffraction [47] and dark-field X-ray microscopy [48]. Therefore, a theoretical strain field was used to predict the displacement field using the proposed method, and the accuracy of the solution was demonstrated by comparing it with the original field through the stress intensity factors.

3.2.1. Analytical dataset

Consider a 3D crack under mixed modes I, II and III. Similarly, using the Westergaard solution for a linear elastic material, the strain field is

$$\varepsilon_{ij} = \frac{1}{2\mu\sqrt{2\pi r}}\left[K_I f_{ij}^{(I)}(\theta,\chi) + K_{II} f_{ij}^{(II)}(\theta,\chi) + K_{III} f_{ij}^{(III)}(\theta,\chi)\right] + O\left(r^{\frac{1}{2}}\right), \quad (19)$$

Following that, the displacement in x and y-directions, u_x and u_y, can be expressed by

$$u_i = \frac{1}{2\mu}\sqrt{\frac{r}{\sqrt{2\pi}}}\left[K_I g_i^{(I)}(\theta,k) + K_{II} g_i^{(II)}(\theta,k) + K_{III} g_i^{(III)}(\theta,k)\right] + O\left(r^{\frac{3}{2}}\right), \quad (20)$$

where g is a dimensionless function that depends on θ and the parameter k.

A 3D cubic domain of L x L x L size was considered such that the crack is parallel to x-axis and its front is located at the centre of the domain (i.e., $a = L/2$) at $x = a, y = 0$, and $z \in [-L/2, L/2]$ as shown in Fig. 3b The strain and displacement components in x, y and z-directions are determined for a domain of $L = 8$ mm and stress intensity factors of $K_I = 30$ MPa·m$^{1/2}$, $K_{II} = 40$ MPa·m$^{1/2}$ and $K_{III} = 10$ MPa·m$^{1/2}$. The isotropic elastic modulus and Poisson's ratio were taken to be $E = 210$ GPa and $\nu = 0.3$. The domain is discretised using a uniform hexahedral mesh of element length $l_e = 0.67$ mm (i.e., total of 1331 elements). In the discretisation, linear interpolation functions are adopted, i.e., 8-node linear element (Fig. 3a). The number of computational points is set to 8, as shown in Fig. 1.

3.2.2. Results and discussion

For the mixed-mode synthetic data, the central mode I equalled 30.4 ± 0.5 MPa m$^{0.5}$, mode II was −38.5 ± 3.2 MPa m$^{0.5}$, mode III was 8.7 ± 0.5 MPa m$^{0.5}$ and the energy release rate of 10,958 ± 1050 J m^{-2} (continuous lines in Fig. 3c). These values are ~4 % lower than the theoretical stress intensity factors used to calculate the synthetic field. This could be attributed to the sensitivity of stress intensity calculation (via the interaction integral method [49]) to the crack tip position, especially for mode I and mode II components [50] and considering the very coarse field. The variance is from the values obtained as the domain of integration expanded from the crack tip. A thorough analysis of this is out of the scope of this paper.

The integrated displacement fields have an average stress intensity factor for mode I loading that equalled 31.7 ± 3 MPa m$^{0.5}$, mode II is −36.8 ± 1.1 MPa m$^{0.5}$, mode III is 8.6 ± 0.2 MPa m$^{0.5}$, and the overall energy release rate of 11,094 ± 52 J m^{-2}. There is good agreement between the overall results and across the sample thickness, as shown in Fig. 3, where the results from the synthetic data are plotted with a continuous line, and points and dotted lines represent the integrated field.

The 3D validation employs synthetic strain fields because current volumetric diffraction-based techniques do not provide dense, uniformly sampled 3D elastic strain maps at the noise level required for controlled benchmarking. The synthetic case verifies the formulation when the full strain tensor is known, while the 2D HR-EBSD example, in Section 3.3, demonstrates robustness under real experimental noise. More details about optimisation can be found in the Supplementary Information.

3.3. HR-EBSD field around a nanoindentation

3.3.1. Methodology

A pre-polished single-crystal Silicon sample was micro-indented on the surface (001) plane at room temperature using a Vickers Diamond Pyramid indenter (136° between faces). A load of 50-gramme force (gf) was applied in 1 s. These conditions are suitable for initiating half-penny cracks with minimal chipping or radial cracks. The indented sample was then fixed to an aluminium stub using conductive paste (i.e., Silver DAG) to minimise image drift and the intensity of blooming caused by electron beam charging. The sample was subsequently attached to a Universal EBSD 70° pre-tilted sample holder and placed inside a Carl Zeiss Merlin field emission gun scanning electron microscope (FEG-SEM). High-quality 800×600-pixel electron backscattering patterns (EBSPs) were collected using a Bruker eFlash CCD camera. The operating parameters were a 20 kV/10 nA beam condition, an 18 mm working distance, a 200 ms exposure time per pattern, 4 × 4 hardware pattern binning, and a 0.25 µm step size.

The topography around the indentation contact impression was

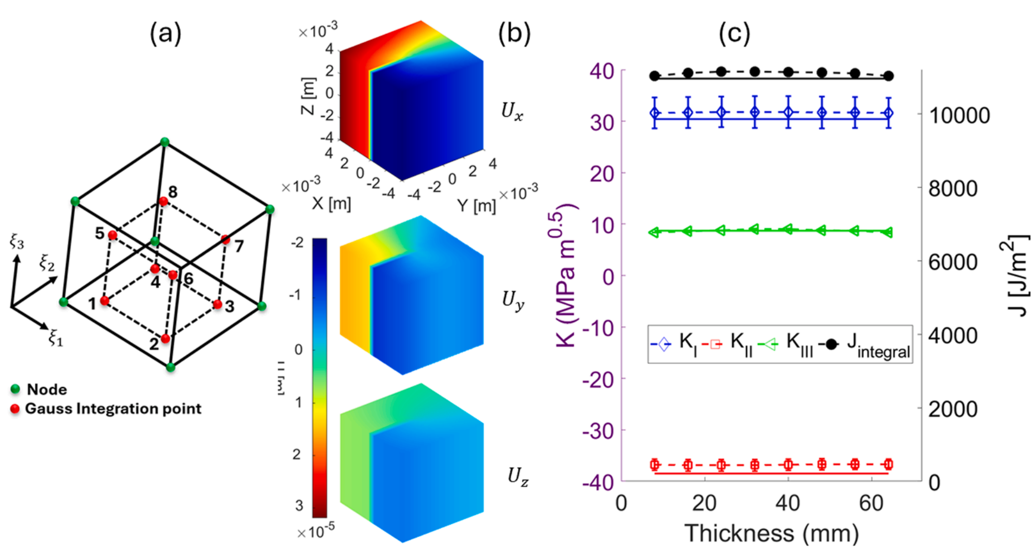

Fig. 3. (a) Schematic of a linear brick element with 8 Gauss points (full integration). A dimensionless local natural coordinate system (ξ_1, ξ_2, ξ_3) was defined by its origin at the centre of the brick element. (b) Synthetic mixed-mode crack field showing displacement in x, y, and z. (c) The stress intensity factor and energy release rate values for synthetic data (continuous line) and the integrated field (point and dotted line) are both calculated in ABAQUS®.

measured using a Veeco AutoProbe (high-resolution) atomic force microscopy (AFM) in contact mode using a 10 nm probe tip with an accuracy of < 1 nm. The scan speed is 0.35 line/*sec* and 15.6 nm step size for an 8 × 8 μm field of view.

The subsurface geometry of the cracks was revealed using Focused Ion Beam (FIB) slicing using a Zeiss Auriga dual-beam SEM-FIB system with a Schottky field emission Gemini electron column and an Orsay Physics "Cobra" Ga^+ ion FIB. The sample was tilted to achieve an eccentricity of 54° before moving to a working distance of 5 mm. The FIB and electron beam coincidence was achieved by adjusting the stage-beam working distance and spatial stage movement, allowing simultaneous milling and secondary electron imaging (SEM). Once the eccentricity and coincidence were achieved, a protective platinum and carbon layers (~1.5 μm thickness of each layer) were deposited using a beam (240 pa/30 kV) to protect the surface, as shown in Fig. 4a. A trapezium trench, 35μm deep, was milled using 16 nA/30 kV to allow for easy viewing of the feature in the third dimension (Fig. 4b). In-lens and Secondary Electron (SE) Imaging conditions with 36° tilt correction (effective 90° viewing) were used for fine milling into the indentation contact impression (green arrow in Fig. 4a) using ATLAS 3D with 600 pA/30 kV milling conditions (Fig. 4c).

The obtained 16-bit image stacks from the FIB slicing each had a voxel size of 10×10×25 nm^3 and examined a volume of 28.29×12.09×23.35 μm^3. 3D image drift was corrected using Fiji ImageJ [51] before manually training a Weka Segmentation classifier [52] on 20 frames to detect cracks from the matrix and the protective Pt layer (Fig. 4d) before applying the trained classifier to the entire image stack. The segmented stack was then processed using AVIZO (version 2020.3.1) to visualise the crack in 3D

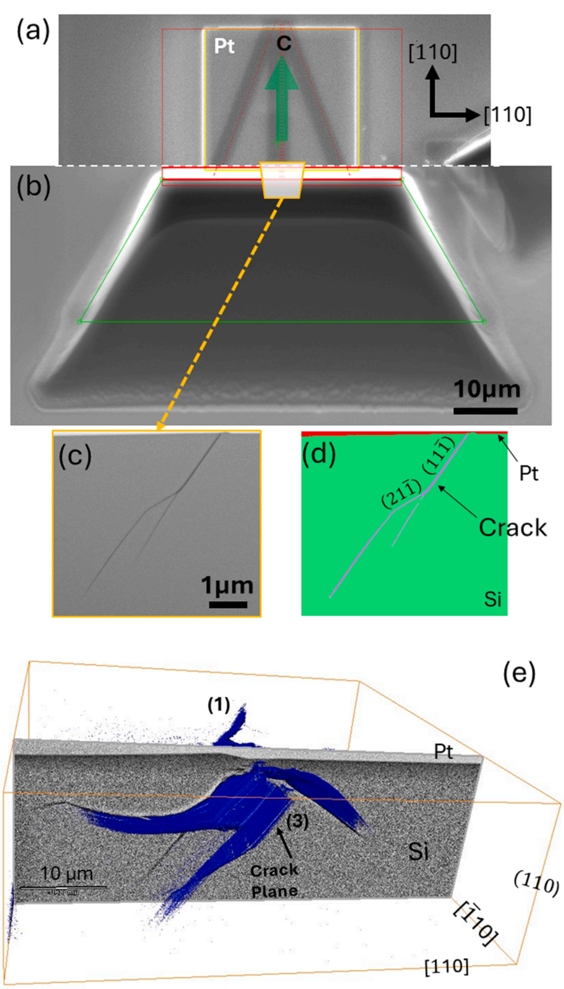

Fig. 4. (a) deposition of protective Platinum (Pt) and Carbon (C) layers. (b) Trapezium trench. (c) SE image for the crack. (d) Segmented crack geometry (purple) in a Silicon (green) covered with a Pt layer (red). (e) Crack geometry as revealed by focused ion beam (see https://shorturl.at/UNlX0).

3.3.2. Indent morphology

One crack emanated from each of the four corners of the Vickers micro-indentation. The cracks were slightly curved near the contact impression, but propagated in a straight line along the [110] and [$\bar{1}$10] directions (x and y-axis, respectively) (Fig. 5a). The 3D observation of the cracks caused by the indentation (Fig. 4e) shows they did not have the same length, straight surface trace, and did not conform to a specific cleavage system, but – in general – may be described as having a Half-penny geometry for the $\langle 110\rangle\{111\}$ cracks labelled (1) and (3) inclined by ~35° from the (110) near the surface and branching into a lateral crack (Fig. 5b) ~3 μm away from the indentation site and deep into the sample. The half-penny crack starts from the expected location of the plastic zone under the indentation impression. The radial geometry for the $\langle 110\rangle\{110\}$ crack labelled (2) and the $\langle 530\rangle\{110\}$ crack (4) also branched to a lateral crack, which can cause chipping. Radial vertical cracks started outside the plastic zone and are shallower than the half-penny cracks. The half-penny geometry of the crack switches between crystal planes, as seen in Fig. 4d, where the crack changes the $(11\bar{1})$ plane to $(21\bar{1})$ plane before going back to the $(11\bar{1})$. Median cracks, parallel to the loading axis and induced due to the outward stress, were observed directly beneath the indentation impression and reached a maximum depth of ~1.1 μm.

The sequence of crack formation with indentation generally starts with median cracks, and once the indent is lifted, leaving a residual impression, the residual tensile stresses cause lateral cracks that may curve upward to meet the surface and cause chipping, whereas the residual hoop stress causes shallow radial cracks [53]. Microcracks generated by stresses from the plastic deformation at the contact impression vicinity coalesce to form a large crack that propagates towards the surface and may influence the radial crack geometry [54] Crack deflection may also be related to the crack propagation velocity [55,56]. These factors all contribute to the irregular crack shape [57].

3.3.3. HR-EBSD analysis

The elastic deformation at the surface (Fig. 5) was calculated using a cross-correlation-based HR-EBSD analysis [13,58] on the collected EBSPs with a reference pattern chosen remotely from the stress concentration [59]. The independent change in interplanar spacing and shifts in zone axes were measured in 30 regions of interest (ROI) in each EBSP with a bicubic interpolation method for the best-fit solution. After the 1st iteration to calculate the local lattice rotation, HR-EBSD analysis was repeated to calculate the strain after remapping the pattern with a rotation matrix constructed from the local lattice rotation [60]. The measured small shifts and distortion between EBSPs and reference EPSP were then related to the elastic displacement gradient (∇u^e) and polarly decomposed to deviatoric strains (symmetric part, where $ij = ji$), ε_{ij}, and lattice rotations (asymmetric part, where $ii = jj = 0$), ω_{ij}. Stress was calculated using (001) Silicon anisotropic elastic constants of $C_{11} = 165.7$, $C_{44} = 79.6$, $C_{12} = 63.9$ in GPa [61]. For 18 dislocation types (12 edge and six screw dislocation systems) of face-centric cubic (FCC) mono-Si crystal, the geometrically necessary dislocation (GND) density was also estimated from the lattice rotation [62].

The high-quality EBSPs yielded a field with an excellent average cross-correlation peak height of 0.87 ± 0.08, and an extremely low mean angular error of $\pm\ 2.82 \times 10^{-4}$ rad (excluding the cracks and indentation itself). The deformation fields are symmetrical around the indentation impression. For example, compressive normal strains can be observed along the x- and y-axes, with in-plane shear stresses positive and negative along the cracks, all indicating a residual crack opening stress field.

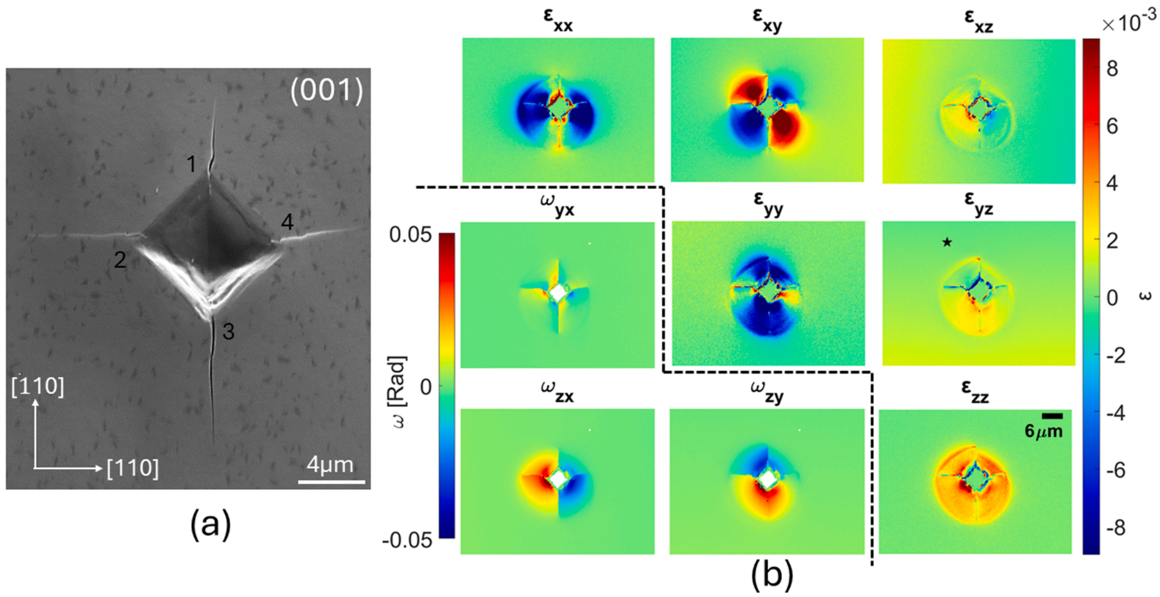

Fig. 5. (a) Secondary electron microscopy (SEM) image for the indentation on the (001) mono-Si crystal. (b) HR-EBSD deviatoric strain and rotation components. The location of the reference $EBSP_0$ is highlighted with a star in $\boldsymbol{\varepsilon_{yz}}$.

The out-of-plane shear strain is minimal, but there is a slight gradient in ε_{yz} and ε_{xz} (Fig. 5b) that, on integration to the displacement field, describes a rigid body rotation. This gradient is due to the uncorrected pattern centre (PC) shift from beam movement during pattern acquisition [63]. The effect of this gradient on the integrated displacements can be removed by assigning the absolute minimum displacement to zero and then taking this as the origin to extract the rotation angles (ψ, θ, ϕ) using Kevin Shoemaker's method [64]. This allows one to construct the transformation matrix (R in Eq. (21)) and correct the displacement field's rigid body movement [65]. Fig. 6a shows the inverse relationship between the induced rigid body rotation and the thickness (Z) of the HR-EBSD information depth.

$$R = \begin{bmatrix} \cos\theta\cos\phi & \cos\theta\sin\phi & -\sin\theta \\ \sin\psi\sin\theta\cos\phi - \cos\psi\sin\phi & \sin\psi\sin\theta\sin\phi + \cos\psi\cos\theta & \cos\theta\sin\psi \\ \cos\psi\sin\theta\cos\phi + \sin\psi\sin\phi & \cos\psi\sin\theta\sin\phi - \sin\psi\cos\phi & \cos\theta\cos\psi \end{bmatrix} \tag{21}$$

The out-of-plane (positive) normal strain distribution (ε_{zz} in Fig. 5b) is similar to out-of-plane surface displacements that have been obtained from optical interference measurements of a Palmqvist crack system [66] and correlate with the calculated GND density distribution (Fig. 6b). The GND density near the indentation impression edges is 7.7 $\pm$ 1.8 $\times$ 10^{12}, decreasing gradually to about 2.7 $\pm$ 0.9 $\times$ 10^{12} m^{-2} with 83 % of the dislocations at $45^\circ/\langle 110\rangle b$ to the surface normal (between 1 and 2 in Fig. 6c) before falling to a background density of 0.3 $\pm$ 0.1 $\times$ 10^{12} m^{-2}. Silicon is a brittle material at room temperature, but when indented, the deformation is accompanied by a competitive process of transformation-induced plasticity [67,68] and dislocation nucleation at the surface [69,70]. As the indenter moves into the sample, uniform material pile-up occurs around the indentation, changing the local orientation and strain compared to undeformed material away from the indenter contact site. The GND represents lattice rotations resulting from crystal distortion and does not necessarily indicate actual plasticity [71]. Thus, the calculated geometrically necessary dislocations (Fig. 8b) represent equivalent dislocations that maintain the material change in orientation. Interestingly, the GND distribution is elliptical and rotated by 1.2° from the edge trace of the indentation (θ in Fig. 6b). This may be due to the indenter being slightly inclined relative to the surface, which would affect the measured field and crack length.

3.3.4. Strain integration

Hexahedral (brick) elements with eight nodes were used to structurally mesh the field, assuming a thickness Z of the membrane layer probed by the backscattered electrons. The model excluded the cracks (Fig. 7a), which were identified by their locally elevated level of GND density (greater than 1.6 $\times$ 10^{13} m^{-2}). The thickness Z was obtained by simulating the EBSP acquisition process using a Monte Carlo Simulation (Casino v2.48 [72]) of the trajectory of 5 million electrons impinging on a bulk Si sample (Fig. 7b) with a beam radius of 25 nm at these conditions [73]. The probabilities of the (EBSP) signal being from a certain depth were binned (Fig. 7c) into differently sized ranges from 1 to 1600 nm, with the mean (50 % probability) at 173 nm and the mode at 40 nm. The strain field was then integrated into the equivalent elastic displacement field for these values of Z, i.e., different ranges of the EBSP information depth.

The profile of the out-of-plane displacement U_z increases towards the indenter centre, similar to the GND density profile discussed earlier. The magnitude of the U_z changed with the assumed membrane thickness, as did the spatial distribution (Fig. 8), although the in-plane displacements (U_x and U_y) were identical in magnitude and did not change with Z. Results for $Z = 700$ nm are shown in Fig. 9b–d. The in-plane displacements (Fig. 9c and d) indicate that the cracks may be under a residual tensile opening. It is generally assumed that once the indenter is removed, the cracks should be minimally loaded [74–76] only by the residual tensile stresses exerted due to the compressed plastic zone. This assumption will be investigated shortly.

The out-of-plane displacement fields, calculated using a range of assumed depth Z, were compared to the topographical profile of the indentation impression measured using AFM. Agreement in magnitude was found both at Z of 700 nm and 16 nm (Fig. 8b), but the distributions agreed best at 700 nm, which is also the depth within which 91.7 % of the signal is produced.

The depth resolution of EBSD is widely accepted to vary between 10 and 40 nm, decreasing with the material's atomic number [77]. Nevertheless, experimental measurement, using a differently thick transparent amorphous layer of Cr coating a mono-Si crystal, indicated that the depth of resolution may be as shallow as 2 nm [78]. However, using a similar experimental approach, different results were reported (Table 1) with no clear trend. For example, Isabell and David [79] concluded that depth resolution in Si could extend to 1 μm due to inelastic scattering (including tangential smearing and channelling effect).

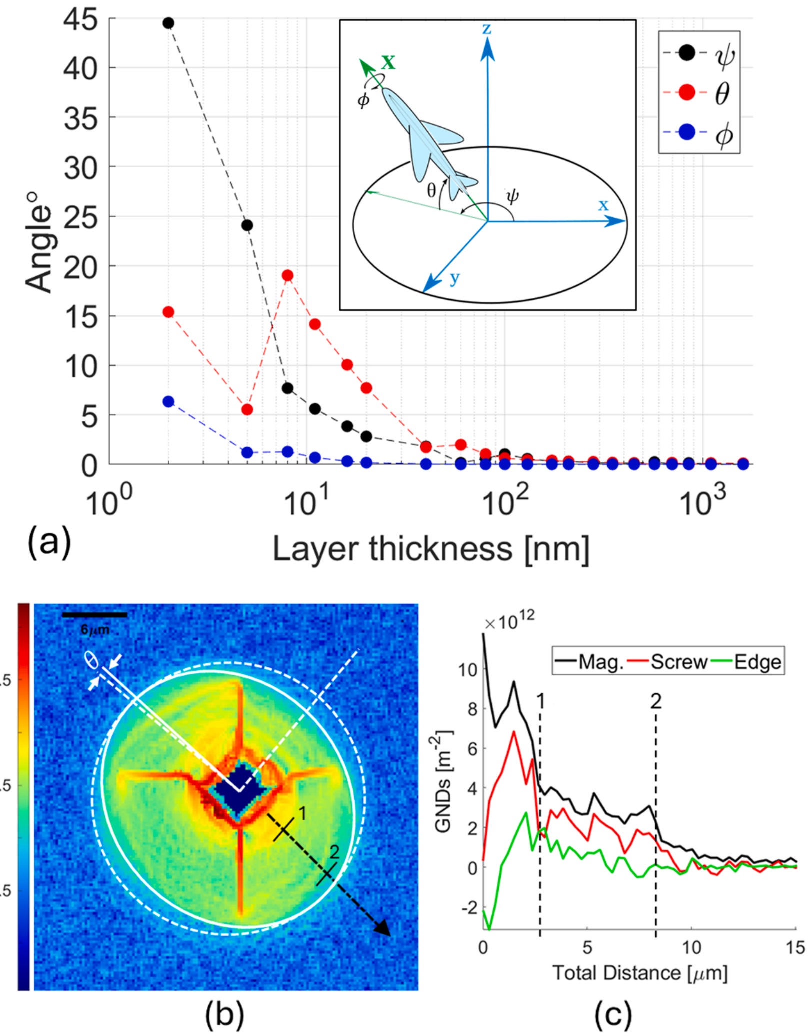

Fig. 6. (a) Corrected rigid body Euler angles (ψ, θ, ϕ) extracted from the out-of-plane shear strain field gradients of Fig. 5b, as a function of the assumed layer thickness, Z, of HR-EBSD information. (b) Estimated geometrically necessary dislocations (GND) density with the theoretical circular profile around the indentation in dashed white lines and the experimental oblique profile in continuous white lines. The angle between the circle and the oblique is θ. The dashed black line is where the GND density line profile shown in (c) is taken, starting from near the indentation impression and going outward.

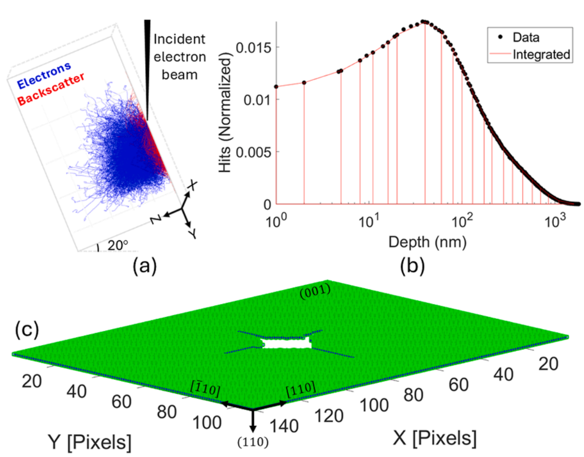

Fig. 7. (a) The membrane layer represents the probed field excluding the crack stem and is meshed using an eight-node Hexahedron element. (b) Monte Carlo simulation of an electron's trajectory. (c) Probability of backscattered electrons.

Thus, the apparent depths of 16 or 700 nm are still reasonable.

MC simulation results appear more consistent, decreasing with material density, as the calculated depth of resolution for EBSPs formation is understood using Bloch wave theory. In this context, backscattered primary electrons, after interacting with the crystal lattice, exit the surface carrying information about the crystallinity of the volume that interacts with the electrons. The backscattered electrons (BSE) energy distribution depends on the material's characteristics and the beam conditions [96]. This BSE wave field is also affected by the thermal diffuse scattering process that causes incoherent and inelastic (energy loss) scattering – after the Bragg diffraction events – which does not, yet, have a complete physical description that can be related to mechanisms that constitute EBSP depth resolution [97,98]. However, there are supporting arguments that MC simulation gives an (accurate [85,93]) approximation that is based on the wrong assumptions [78].

On the contrary, the experimental results in Table 1 are not consistent. These experiments are highly cumbersome due to the need for highly precise and well-calibrated equipment, with the results open to interpretation [99]. This is mainly because there is no agreement about the definition/criteria of depth resolution. For example, definitions that are dependent on where ~92 % of the signal is generated [100,101], pattern quality [78], or as ambiguous as "where useful information is obtained" [102]. All reported values in Table 1 either do not provide a

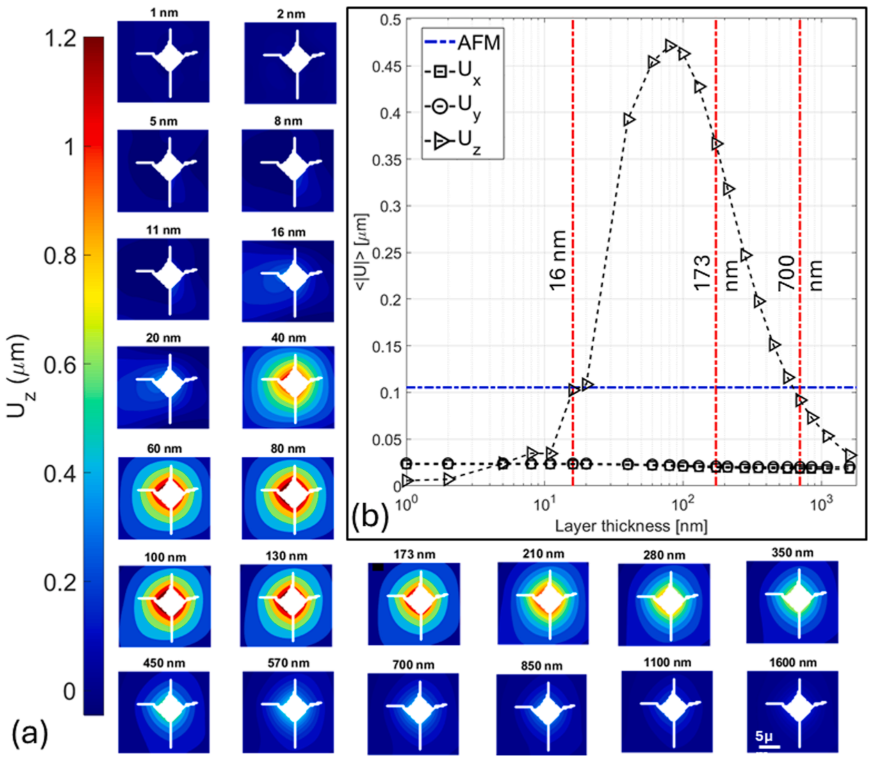

Fig. 8. Displacement Integration assumes a different membrane (Z) thickness, illustrated as (a) Uz maps and (b) absolute average. The absolute average of the integrated displacement fields was calculated from a 25×25 μm² window centred around the indent to match the AFM window.

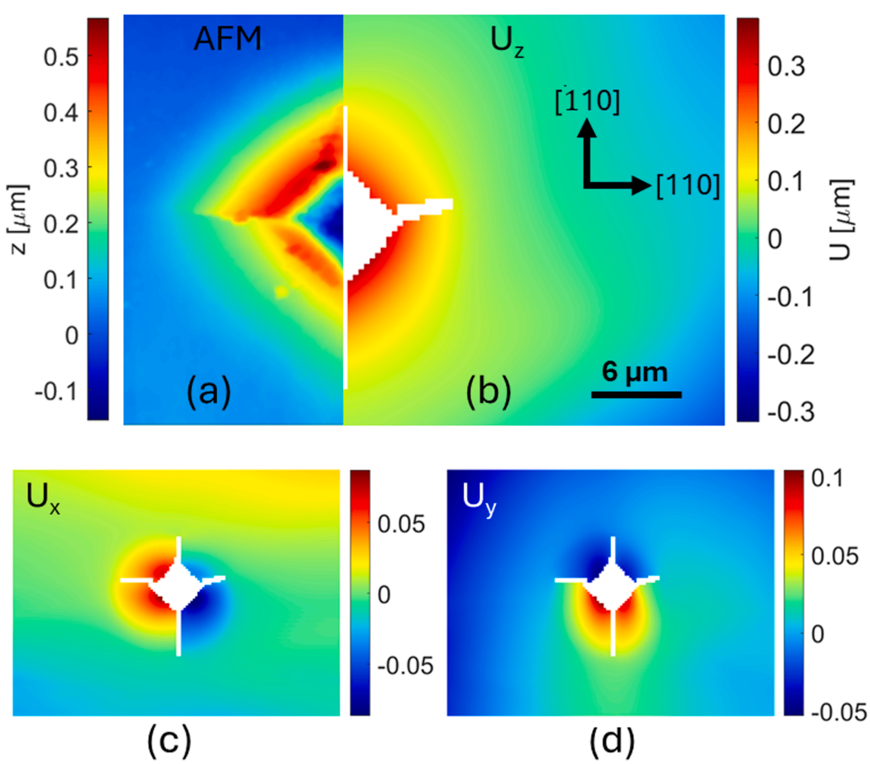

Fig. 9. (a) AFM measured topography around the indentation impression. Integrated (b) U_z, (c) U_x and (d) U_y elastic displacement calculated while assuming 700 nm depth (Z).

definition or lack a rationale for the definition. In addition, most of these experiments do not mention the beam size, tilt angle, beam to sample and sample to detector working distance, and – sometimes – even the beam energy, which are critical parameters for determining (or simulating) the depth resolution of the patterns as the interaction volume increases with beam energy and size and decreases with the sample

Table 1
Measured EBSP depth resolution from experiments and Monte Carlo (MC) based simulation to infer EBSP depth resolution. Density was measured at room temperature.

Author	Material	Density (kg/m^3)	Voltage (kV)	Depth Resolution (nm)
Dingley [77]	–	–	–	10–40
Dingley and Randle [80]	–	–	–	10
El-Dasher et al. [81]	–	–	–	~20
Bhattacharyya and Eades [82]	–	–	–	< 1000 (MC)
Zaefferer [78]	Si	2.33	15	3.5 ± 1.5
Yamamoto [83]	Al	2.70	20	50
Bhattacharyya and Eades [82]	Al	2.70	20	15–40
Baba-Kishi [84]	Al	2.70	20	> 50
Ren et al. [85]	Al	2.70	20	115 (MC)
Isabell and Dravid [79]	Al	2.70	30	~400
Michael and Goehner [86,87]	Al	2.70	40	100
Yamamoto [83]	Al	2.70	50	120
Isabell and Dravid [79]	Nb	3.58	30	< 1000
Isabell and Dravid [79]	$SrTiO_3$	5.11	30	~300
Keller et al. [88]	GaAs	5.32	15	30
Steinmetz and Zaefferer [89]	Fe	7.87	7.5	10
Bordín et al. [90]	σ-Fe	7.87	20	16 (MC)
C. Zhu et al. [91]	Ni	8.91	10	10 (MC)
Harland et al. [92][2]	Ni	8.91	30	$\lesssim$ 10
Kohl [79,93]	Ni	8.91	30	5–6 (MC)
Michael and Goehner [86,87]	Ni	8.91	40	20
Chen et al. [94]	Cu	8.96	5	38
Chen et al. [94]	Cu	8.96	10	46
Yamamoto [83]	Cu	8.96	20	20
Ren et al. [85]	Cu	8.96	20	35 (MC)
Chen et al. [94]	Cu	8.96	30	72
Yamamoto [83]	Cu	8.96	50	50
Ren et al. [85]	Ag	10.49	20	30 (MC)
Isabell and Dravid [79]	W	19.30	30	~50
Ren et al. [85]	Au	19.30	20	22 (MC)
Harland et al. [95]	Au	19.30	30	80
Michael and Goehner [86,87]	Au	19.30	40	10

[2] Using a small-angle detector.

atomic number or density [79]. Also, the beam current is not considered a parameter that affects the depth resolution, either in experimental or simulation settings. However, it affects the beam spot size and the pattern signal-to-noise (S/N) ratio [91,103,104]. Most importantly, conclusions drawn from both experiments and simulations assumed the surface is pristine and that the depth resolution is heterogeneous, which is not valid for a deformed sample [78].

Determining the depth resolution is still challenging, as it was made clear from the contradicting depth resolution reported in the literature; thus, we will assume the depth resolution as 700 nm (where 91.7 % of the information is coming from, Fig. 7c) considering that this depth resolution yields (elastic) out-of-plane displacement similar to AFM.

The robustness of the integration against experimental artefacts is further demonstrated in the Supplementary Information, which includes additional optimisation methods to account for noise and missing points. For more information about how noise and HR-EBSD reference patterns affect fracture parameters, please refer to [105] and [39,106], respectively.

3.3.5. Calculating fracture parameters

To characterise the indentation cracks, we use the elastic strain field obtained from HR-EBSD to calculate the stress intensity factors for the inclined $(11\overline{1})$ crack labelled (3) and the orthogonal $(\overline{1}10)$ crack labelled (2). The three-dimensional stress intensity factors (SIFs) can be extracted using the interaction integral natively implemented in ABAQUS® finite element solve, which uses the displacement field obtained from integrating the elastic strains at a 700 nm depth of information as a boundary condition and the material's elastic stress-strain relationship [33]. Plane stress conditions were assumed by considering the thin probed layer and that the sample is not constrained at the surface; thus, it deforms freely in the third dimension [107]. The interaction integral approach – as implemented in ABAQUS® – is robust [50] and less sensitive to the crack position compared to field fitting approaches [108].

The field at crack 3 (the $(11\overline{1})$ crack, Fig. 10) was mainly compressive ε_{xx}, with a minimal ε_{yy} (localised at the crack tip) and a uniform in-plane shear strain along the crack. The strains ε_{xx} and ε_{zz} uniformly encapsulated the crack (Fig. 10a). The analysis of the field, when calculated for integration contours where convergence stabilised (shaded area in Fig. 10b), obtained a total mode I stress intensity factor (K_I^T) of 0.02 ± 0.00 MPa $m^{0.5}$, including the in-plane component of mode I (K_I) that equals 0.01 ± 0.00 MPa $m^{0.5}$, in-plane mode II shear (K_{II}) of −0.38 ± 0.00 MPa $m^{0.5}$, and out-of-plane mode III shear (K_{III}) of −0.38 ± 0.01 MPa $m^{0.5}$. Because the HR-EBSD field represents a residual elastic field, a negative or vanishing mode I indicates the absence of residual opening, and the existence of a compressive field at the crack tip that is closing the crack. The signs of the shear components (K_{II} and K_{III}) depend solely on mesh-based nodal ordering and are not physically meaningful [109]. Therefore, the crack exhibits residual shear loading in a direction inclined to the indented surface, with a negligible opening load.

On the other hand, crack 2 (the $(\overline{1}10)$ crack, Fig. 11) has a field with similar in-plane and out-of-plane shear strain but without an apparent strain ε_{yy} localisation at the crack tip. The strains ε_{xx} and ε_{zz} are also not uniformly distributed around the crack. The crack plane is orthogonal to the surface and is loaded by a K_I^T of −0.31 ± 0.04 MPa $m^{0.5}$, K_I of −0.19 ± 0.03 MPa $m^{0.5}$, K_{II} of 0.26 ± 0.02 MPa $m^{0.5}$, and K_{III} of −0.66 ± 0.01 MPa $m^{0.5}$.

The higher out-of-plane mode III (K_{III}) and the out-of-plane component of mode I (K_I^T) in these examples, inflate the value of the strain energy release rate (J-integral) to extend it so that it can be higher than those measured for loaded cracks [110]. This is because K_{III} and K_I^T are dependent on the depth resolution and the size of the integrated window [106]. Thus, these values should be dismissed unless correction methods are developed to address these dependencies. Additionally, because the assumed information depth influences only the out-of-plane displacement component, and this dependency has already been quantified and validated against AFM measurements, any resulting variation in the fracture parameters, namely K_{III} and K_I^T, is bounded by the same uncertainty, and does not require a separate sensitivity analysis.

Although it is somewhat speculative to conclude from these analyses; the observation of mode I in the crack (2), which is orthogonal to the surface, and the higher mode II of crack (3), which is inclined to the surface, is interesting. This difference in the mechanical conditions ahead of these cracks may be due to the orientation of the crack plane geometry relative to the indentation. Both cracks have the same directional Young's modulus and Poisson's ratio [61] due to similar forces from the indentation. The difference in crack planes between cracks (2) and (3) is speculated to be due to the relationship between the plane normalised stress and the plane fracture toughness, i.e., for crack (2) $\sigma_{\perp\{110\}}/K_{Ic\{110\}} > \sigma_{\perp\{111\}}/K_{Ic\{111\}}$ [111] and surface cracks, mixed modality may be due to stress relaxation from lateral cracking [112].

Considering the crack shape, the measured surface mechanical conditions will change with depth; an in situ three-dimensional strain map will be optimal for fully characterising the crack field and properly linking it to geometry, especially in materials where the local fracture

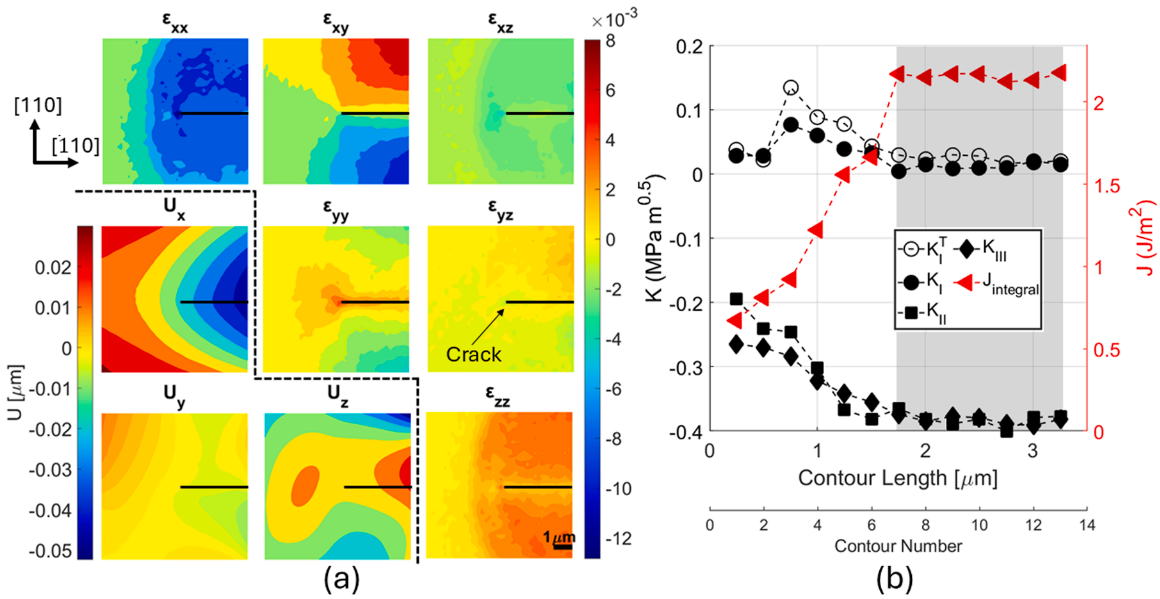

Fig. 10. (a) Elastic strain and displacement fields for $(11\overline{1})$ crack number 3 in Fig. 5a. Displacement was integrated, assuming a 700 nm depth resolution. (b) *J*-integral and stress intensity factors were calculated from the crack field.

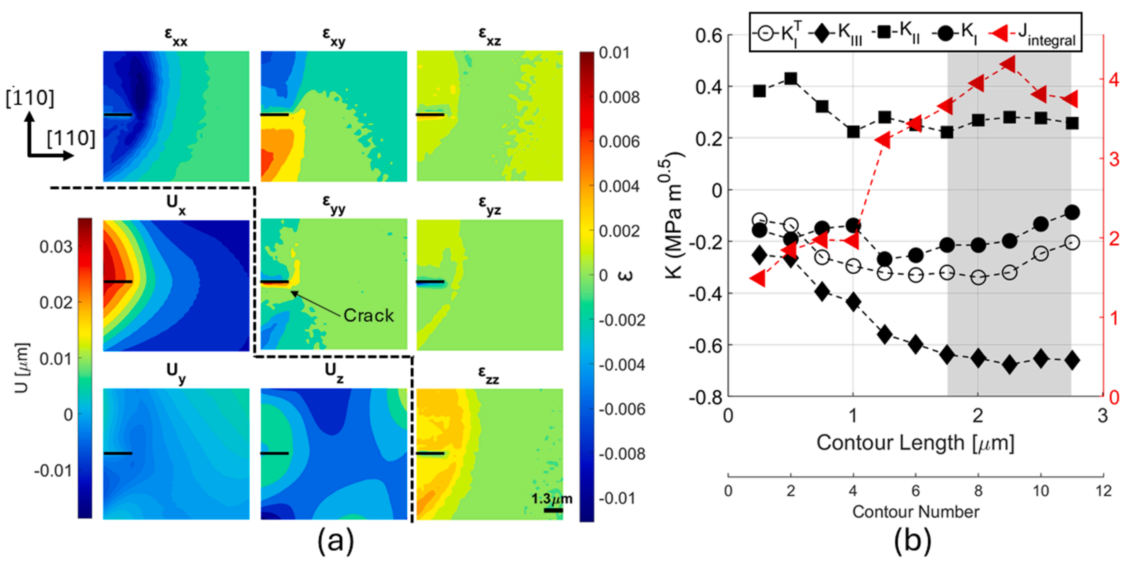

Fig. 11. (a) Elastic strain and displacement fields for $(\overline{1}10)$ crack number 2 in Fig. 5a. Displacement was integrated, assuming a 700 nm depth resolution. (b) *J*-integral and stress intensity factors were calculated from the crack field.

behaviour needs further investigation. In principle, this could be achieved by a 3D strain measurement technique, such as Laue microdiffraction [47], performed in situ, or it could be done using in situ EBSD with a sample geometry that allows examination of the crack under load, such as indentation close to an edge (see [113]). Thus, the method discussed here can be used with (three-dimensional [47,48, 112]) local deformation measurement to calculate fracture toughness without detailed knowledge of the indentation deformation process or the crack length; thus, it can analyse short cracks that do not fit the Lawn-Evans-Marshall (LEM) model.

4. Potential applications

4.1. Fracture at the micro-scale

Fracture toughness at the microscale (e.g., of brittle coatings, particles and hard surfaces) is typically estimated by analysis of indentation-induced cracking via empirical equations, with assumptions of the crack geometry [114–116] and the loading history of the crack tip during indentation [75]. For example, as we showed in the last example, Lawn *et al.* [117–120] indicated that the mode I fracture toughness (K_{IC}) can be estimated for a half-penny-shaped crack that is induced by Vickers indentation with knowledge of the contact impression radius (a), the surface crack length (l), Young's modulus (E), Hardness (H), and maximum indenter load (P), where x_v, is a fitting factor with a value of 0.015 ± 0.007 [115,121]. Dukino and Swain [122] later modified Eq. (22) for Berkovich indentation.

$$K_{IC} = x_v\left(\frac{E}{H}\right)^{1/2}\frac{P}{c^{3/2}},\ c = l + a \tag{22}$$

One potential drawback of using indentation to assess toughness is the uncertainty of the true subsurface crack shape, as the Palmqvist cracks that can initiate from the indentation impression corners [66]) appear similar to median or radial cracks [120]. The significant range of x_v also leads to some inconsistency (and forced consistency [123]) in the toughness values obtained using indentation. One in-depth review [124] concluded that – even for a highly finished surface – the indentation fracture method has "poor value" due to large scatter and user bias, and some believe that fracture toughness determined using indentation should not be accepted, and such data can only be used for comparative purposes [125]. Some of the issues – especially for anisotropic brittle materials – include dependency on the indenter tip angle [126–128], crack deflection [57,129], indentation depth/load dependency [130], and the effects of surface pile-up and size-dependent plastic deformation [131]. For further critical reviews on the indentation fracture method, see [132–134].

More importantly, indentation cracking is a complex phenomenon, as illustrated by the case of silicon at room temperature. Silicon can deform in compression through a high-pressure phase transformation from a diamond cubic structure (Si-I phase) to a body-centred tetragonal structure (β-Si or Si-II phase). The change in stress field with the application and removal of the indenter leads to elastic 'pop-in' and 'pop-out' by transformation-induced plasticity to the cubic BC8 (α-Si or Si-III phase) or rhombohedral R8 structure (Si-XII). Cracking occurs due to the resulting strain mismatch [67,68]. Furthermore, the cracks that develop at the microscale within single grains on specific cleavage planes, or along grain boundaries, are not necessarily oriented perpendicular to the indented surface and may propagate under mixed-mode conditions. Thus, what we have developed in the previous example can be used to quantify the fracture toughness of nanoindentation-induced cleavage cracks, providing alternatives to micro-pillar and cantilever experiments, the indentation fracture method, and analytical solutions.

4.2. Beyond fracture

The J-integral was extensively used in conjunction with surface measurements; however, volumetric quantification coupled with this approach may provide insights into the criteria for deformation-twin [105]/slip-band [106]/micro-cracks propagation [135], as well as twin/slip thickening and twin variant selection. The method is of interest because, firstly, the J-integral can be calculated directly from experimental data without resorting to crystal plasticity models or knowledge of the loading condition or specimen geometry. Secondly, the mechanical condition of a twin can be readily obtained by decomposing the J-integral into opening and shear modes, which are described as stress intensity factors [3,6,33]. Thirdly, the nature of the J-integral facilitates the employment of finite element analysis, and its evaluation is implemented natively in most FE solvers. Furthermore, the experimental strain-integrated displacement field used in the J-integral assessment can be easily incorporated with crystal plasticity models, which can simulate twin growth via the extended finite element method (XFEM [136,137]). Such analyses would benefit from advanced strain energy integral definitions that can be applied to linear elastic and elastic-plastic materials to address factors, including surface traction [138], loading and internal tractions [139], thermal [140] and electrochemical [141], residual stresses [142] and boundary interactions [143–145], which are natively implemented in commercial Finite element software.

Other path-independent conservation integrals are evaluated over a surface that encloses a defect [146,147] can be used to represent a configurational force measured around defects, as most of the information required for computing these integrals is either directly obtained from local measurements or can be approximated (i.e., integrating strains to obtain displacements). For example, the elastic field at a dislocation can be measured using HR-TKD [148] and analysed using the J-, M-[2] and L-integrals [149–151], dislocations arrangement measured using high-resolution synchrotron diffraction [152] can be parameterised using M-integral [153], misfitting inclusions and voids measured using HR-EBSD [154,155] can be evaluated using the Eshelby integral [156], M-integral [157], and pile-ups ahead of the slip band impinged at grain boundaries measured using HR-EBSD [158] or Laue micro-diffraction combined with differential aperture microscopy (DAXM) [159] and analysed using the vectorial J-integral to predict the slip system to nucleate [147].

Furthermore, considering the analysed stress concentration, the measured surface mechanical conditions will change with depth; an in situ three-dimensional strain map will be optimal to fully characterise the concentration field and properly link it to geometry, especially in materials where the local fracture behaviour needs further investigation and the material does not have a trackable volumetric structure suitable for digital volume correlation (DVC). This can be achieved using DAXM for depth-resolved 3D X-ray microscopy at the 34-ID-E beamline, the Advanced Photon Source (APS) [47], or dark-field X-ray microscopy available at the European Synchrotron Radiation Facility (ESRF) [48].

5. Conclusion

This work establishes a general finite-element framework that reconstructs displacement fields directly from experimentally measured elastic strains, removing the dependence on unknown boundary conditions or applied loads. By casting strain integration as an overdetermined least-squares problem, the method delivers stable solutions for both two- and three-dimensional fields. Validation against analytical crack-tip solutions demonstrates that the reconstructed displacements and corresponding stress intensity factors match theoretical values with high accuracy. Application to HR-EBSD measurements around Vickers-induced cracks in monocrystalline silicon confirms that the method can accommodate realistic experimental noise while reproducing independent topographic measurements and resolving local mixed-mode residual loading.

The approach, therefore, provides a practical route to convert high-resolution strain measurements into mechanically meaningful fracture parameters, enabling quantitative assessment of microscale cracks in complex materials. Its formulation is compatible with diffraction-based three-dimensional strain mapping techniques and in situ experiments, making it suitable for studying evolving damage processes, short cracks, and microstructural features that cannot be characterised reliably through conventional indentation-based toughness methods or analytical assumptions. The framework thus opens the way for systematic integration of local strain microscopy with fracture mechanics across multiple length scales.

The code associated with this work is available at 10.5281/zenodo.6411572.

CRediT authorship contribution statement

Abdalrhaman Koko: Writing – original draft, Visualization, Software, Methodology, Investigation, Formal analysis, Conceptualization. **Elsiddig Elmukashfi:** Writing – original draft, Software, Methodology, Conceptualization. **Phani S. Karamched:** Visualization, Software, Investigation. **T. James Marrow:** Writing – review & editing,

[2] The M-integral and the interaction (I) integral are two different integrals that are usually confused in the literature. M-integral describes the energy release rate for uniform expansion of a defect, and I-integral is used for SIFs extraction from the J-integral, assuming small-scale yielding.

Supervision, Resources, Funding acquisition.

Declaration of competing interests

The authors declare that they have no known competing financial interests or personal relationships that could have appeared to influence the work reported in this paper.

Acknowledgements

We thank Professor Peter Wilshaw (University of Oxford) for providing the specimen material and Alexander J. Leide (United Kingdom Atomic Energy Authority) for assistance with nanoindentation. The authors acknowledge the use of experimental equipment from the Oxford Materials Characterisation Service (OMCS) and characterisation facilities within the David Cockayne Centre for Electron Microscopy (DCCEM), Department of Materials, University of Oxford, alongside financial support provided by the Henry Royce Institute (Grant ref EP/R010145/1). Abdalrhaman Koko thanks the Engineering and Physical Sciences Research Council (EPSRC) for providing a PhD studentship (Grant ref EP/N509711/1).

Supplementary materials

Supplementary material associated with this article can be found in the online version at doi:10.1016/j.actamat.2025.121818.

References

[1] R.W. Armstrong, S.D. Antolovich, J.R. Griffiths, J.F. Knott, Fracturing across the multi-scales of diverse materials, Philos. Trans. Royal Soc. A: Math., Phys. Eng. Sci. 373 (2015) 20140474, https://doi.org/10.1098/rsta.2014.0474.

[2] T.M. Brugo, I. Campione, G. Minak, Investigation by digital image correlation of mixed-mode I and II fracture behavior of polymeric IASCB specimens with additive manufactured crack-like notch, Materials. (Basel) 14 (2021) 1084, https://doi.org/10.3390/ma14051084.

[3] A. Koko, T.H. Becker, Mixed-mode fracture: combination of Arcan fixture and stereo-DIC, Theor. Appl. Fract. Mech. (2024) 104724, https://doi.org/10.1016/j.tafmec.2024.104724.

[4] A. Koko, P. Earp, T. Wigger, J. Tong, T.J. Marrow, J-integral analysis: an EDXD and DIC comparative study for a fatigue crack, Int. J. Fatigue 134 (2020) 105474, https://doi.org/10.1016/j.ijfatigue.2020.105474.

[5] T.H. Becker, M. Mostafavi, R.B. Tait, T.J. Marrow, An approach to calculate the J -integral by digital image correlation displacement field measurement, Fatigue Fract. Eng. Mater. Struct. 35 (2012) 971–984, https://doi.org/10.1111/j.1460-2695.2012.01685.x.

[6] M.R. Molteno, T.H. Becker, Mode I-III decomposition of the J -integral from DIC displacement data, Strain 51 (2015) 492–503, https://doi.org/10.1111/str.12166.

[7] T.H. Becker, Extracting fracture properties from digital image and volume correlation displacement data: a review, Strain (2023), https://doi.org/10.1111/str.12469.

[8] Marrow J., Scotson D., Jin X., Chen H., Chen Y., Koko A., et al. Small-specimen testing, with image-based analysis, for crack propagation resistance in polygranular nuclear graphite. graphite testing for nuclear applications: the validity and extension of test methods for material exposed to operating reactor environments, ASTM International100 Barr Harbor Drive, PO Box C700, West Conshohocken, PA 19428-2959; 2022, p. 1–17. 10.1520/STP163920210051.

[9] A. Koko, S. Singh, S. Barhli, T. Connolley, N.T. Vo, T. Wigger, et al., 3-Dimensional analysis of fatigue crack fields and crack growth by in situ synchrotron X-ray tomography, Int. J. Fatigue 170 (2023) 107541, https://doi.org/10.1016/j.ijfatigue.2023.107541.

[10] T.B. Britton, J.L.R.R. Hickey, Understanding deformation with high angular resolution electron backscatter diffraction (HR-EBSD), IOP. Conf. Ser. Mater. Sci. Eng. 304 (2018) 012003, https://doi.org/10.1088/1757-899X/304/1/012003.

[11] D. Wallis, L.N. Hansen, T.B. Britton, A.J. Wilkinson, High-angular resolution electron backscatter diffraction as a new tool for mapping lattice distortion in geological minerals, J. Geophys. Res. Solid. Earth. 124 (2019) 6337–6358, https://doi.org/10.1029/2019JB017867.

[12] T.B. Britton, A.J. Wilkinson, High resolution electron backscatter diffraction measurements of elastic strain variations in the presence of larger lattice rotations, Ultramicroscopy 114 (2012) 82–95, https://doi.org/10.1016/J.ULTRAMIC.2012.01.004.

[13] A.J. Wilkinson, G. Meaden, D.J. Dingley, High-resolution elastic strain measurement from electron backscatter diffraction patterns: new levels of sensitivity, Ultramicroscopy 106 (2006) 307–313, https://doi.org/10.1016/j.ultramic.2005.10.001.

[14] A. Koko, V. Tong, A.J. Wilkinson, T.J. Marrow, An iterative method for reference pattern selection in high-resolution electron backscatter diffraction (HR-EBSD), Ultramicroscopy 248 (2023) 113705, https://doi.org/10.1016/j.ultramic.2023.113705.

[15] L. Clément, R. Pantel, L.F.T. Kwakman, J.L. Rouvière, Strain measurements by convergent-beam electron diffraction: the importance of stress relaxation in lamella preparations, Appl. Phys. Lett. 85 (2004) 651–653, https://doi.org/10.1063/1.1774275.

[16] K. Usuda, T. Numata, T. Irisawa, N. Hirashita, S. Takagi, Strain characterization in SOI and strained-Si on SGOI MOSFET channel using nano-beam electron diffraction (NBD), Mater. Sci. Eng.: B 124–125 (2005) 143–147, https://doi.org/10.1016/J.MSEB.2005.08.062.

[17] M.J. Hÿtch, E. Snoeck, R. Kilaas, Quantitative measurement of displacement and strain fields from HREM micrographs, Ultramicroscopy. 74 (1998) 131–146, https://doi.org/10.1016/S0304-3991(98)00035-7.

[18] E. Guerrero, P.L. Galindo, A. Yáñez, J. Pizarro, M.P. Guerrero-Lebrero, S. I. Molina, Accuracy assessment of strain mapping from Z -contrast images of strained nanostructures, Appl. Phys. Lett. 95 (2009), https://doi.org/10.1063/1.3243990/338165.

[19] R.V. Martins, L. Margulies, S. Schmidt, H.F. Poulsen, T. Leffers, Simultaneous measurement of the strain tensor of 10 individual grains embedded in an Al tensile sample, Mater. Sci. Eng.: A 387–389 (2004) 84–88, https://doi.org/10.1016/j.msea.2004.02.069.

[20] J. Oddershede, S. Schmidt, H.F. Poulsen, H.O. Sørensen, J. Wright, W. Reimers, Determining grain resolved stresses in polycrystalline materials using three-dimensional X-ray diffraction, J. Appl. Crystallogr. 43 (2010) 539–549, https://doi.org/10.1107/S0021889810012963.

[21] A. King, G. Johnson, D. Engelberg, W. Ludwig, J. Marrow, Observations of intergranular stress corrosion cracking in a grain-mapped polycrystal, Science (1979) 321 (2008) 382–385, https://doi.org/10.1126/science.1156211.

[22] B.C. Larson, W. Yang, G.E. Ice, J.D. Budai, J.Z. Tischler, Three-dimensional X-ray structural microscopy with submicrometre resolution, Nature 415 (2002) 887–890, https://doi.org/10.1038/415887a.

[23] L.E. Levine, B.C. Larson, W. Yang, M.E. Kassner, J.Z. Tischler, Delos-Reyes MA, et al., X-ray microbeam measurements of individual dislocation cell elastic strains in deformed single-crystal copper, Nat. Mater. 5 (8) (2006) 619–622, https://doi.org/10.1038/nmat1698, 2006;5.

[24] S. Maddali, J.S. Park, H. Sharma, S. Shastri, P. Kenesei, J. Almer, et al., High-energy coherent x-ray diffraction microscopy of polycrystal grains: steps toward a multiscale approach, Phys. Rev. Appl. 14 (2020) 024085, https://doi.org/10.1103/PHYSREVAPPLIED.14.024085/FIGURES/11/MEDIUM.

[25] R. Harder, I.K. Robinson, Coherent X-ray diffraction imaging of morphology and strain in nanomaterials, JOM 65 (2013) 1202–1207, https://doi.org/10.1007/s11837-013-0682-4.

[26] J.V. Bernier, R.M. Suter, A.D. Rollett, J.D. Almer, High-energy X-ray diffraction microscopy in materials science, Annu Rev. Mater. Res. 50 (2020) 395–436, https://doi.org/10.1146/annurev-matsci-070616-124125.

[27] P. Jenčuš, J. Polák, P. Lukáš, O. Muránsky, In situ neutron diffraction study of the low cycle fatigue of the α−γ duplex stainless steel, Physica B Condens. Matter. 385–386 (2006) 597–599, https://doi.org/10.1016/J.PHYSB.2006.06.109.

[28] R. Barabash, Y. Gao, Y. Sun, S.Y. Lee, H. Choo, P.K. Liaw, et al., Neutron and X-ray diffraction studies and cohesive interface model of the fatigue crack deformation behavior, Philos. Mag. Lett. 88 (2008) 553–565, https://doi.org/10.1080/09500830802311080.

[29] T. Lorentzen, T. Leffers, Strain Tensor Measurements by Neutron Diffraction. Measurement of Residual and Applied Stress Using Neutron Diffraction, Springer Netherlands, Dordrecht, 1992, pp. 253–261, https://doi.org/10.1007/978-94-011-2797-4_16.

[30] J.R. Rice, Some remarks on elastic crack-tip stress fields, Int. J. Solids. Struct. 8 (1972) 751–758, https://doi.org/10.1016/0020-7683(72)90040-6.

[31] J.R. Rice, A path independent integral and the approximate analysis of strain concentration by notches and cracks, J. Appl. Mech. 35 (1968) 379–386, https://doi.org/10.1115/1.3601206.

[32] J.R. Rice, G.F. Rosengren, Plane strain deformation near a crack tip in a power-law hardening material, J. Mech. Phys. Solids. 16 (1968) 1–12, https://doi.org/10.1016/0022-5096(68)90013-6.

[33] A. Koko, J. Marrow, DIC2Abaqus: calculating mixed-mode stress intensity factors from 2D and 3D-stereo displacement fields, SoftwareX. 31 (2025) 102231, https://doi.org/10.1016/j.softx.2025.102231.

[34] A. Koko, D. Salim, N. Leung, N. Spetsieris, S. Smith, D. England, et al., Exploring short crack behaviour and fracture transition in 5052 aluminium alloy, Results. Eng. (2025) 105303, https://doi.org/10.1016/j.rineng.2025.105303.

[35] M. Mokhtarishirazabad, P. Lopez-Crespo, B. Moreno, A. Lopez-Moreno, M. Zanganeh, Evaluation of crack-tip fields from DIC data: a parametric study, Int. J. Fatigue 89 (2016) 11–19, https://doi.org/10.1016/j.ijfatigue.2016.03.006.

[36] J.R. Yates, M. Zanganeh, Y.H. Tai, Quantifying crack tip displacement fields with DIC, Eng. Fract. Mech. 77 (2010) 2063–2076, https://doi.org/10.1016/j.engfracmech.2010.03.025.

[37] B.N. Datta, Numerical linear algebra and applications. 3600 market street, 6th floor philadelphia, in: PA 19104-2688, SIAM, 2010, https://doi.org/10.1137/1.9780898717655.

[38] V. Tong, J. Jiang, A.J. Wilkinson, Britton T Ben, The effect of pattern overlap on the accuracy of high resolution electron backscatter diffraction measurements, Ultramicroscopy. 155 (2015) 62–73, https://doi.org/10.1016/j.ultramic.2015.04.019.

[39] A. Koko, T.H. Becker, E. Elmukashfi, N.M. Pugno, A.J. Wilkinson, T.J. Marrow, HR-EBSD analysis of in situ stable crack growth at the micron scale, J. Mech. Phys. Solids. 172 (2023) 105173, https://doi.org/10.1016/j.jmps.2022.105173.

[40] S.M. Barhli, L. Saucedo-Mora, C. Simpson, T. Becker, M. Mostafavi, P.J. Withers, et al., Obtaining the J-integral by diffraction-based crack-field strain mapping, Procedia Struct. Integrity 2 (2016) 2519–2526, https://doi.org/10.1016/j.prostr.2016.06.315.

[41] T.F. Coleman, Y. Li, An interior Trust region approach for nonlinear minimization subject to bounds, SIAM J. Optim. 6 (1996) 418–445, https://doi.org/10.1137/0806023.

[42] S.M. Barhli, Advanced Quantitative Analysis of Crack fields, Observed by 2D and 3D Image correlation, Volume Correlation and Diffraction Mapping, University of Oxford, 2017. Ph.D.

[43] H.M. Westergaard, Bearing pressures and cracks: bearing pressures through a slightly waved surface or through a nearly flat part of a cylinder, and related problems of cracks, J. Appl. Mech. 6 (1939) A49–A53, https://doi.org/10.1115/1.4008919.

[44] K.-J. Bathe, Appropriate order of numerical integration. Finite Element Procedures, 2nd ed., 2016, pp. 465–476.

[45] P.G. Ciarlet, The finite element method for elliptic problems, Soc. Indust. Appl. Math (2002), https://doi.org/10.1137/1.9780898719208.

[46] B.A. Szabo, A. Barna, Babuška Ivo, Finite Element Analysis, 1st ed., John Wiley & Sons, 1991.

[47] A.A. MacDowell, R.S. Celestre, N. Tamura, R. Spolenak, B. Valek, W.L. Brown, et al., Submicron X-ray diffraction, Nucl. Instrum. Methods Phys. Res. a 467–468 (2001) 936–943, https://doi.org/10.1016/S0168-9002(01)00530-7.

[48] M. Kutsal, P. Bernard, G. Berruyer, P.K. Cook, R. Hino, A.C. Jakobsen, et al., The ESRF dark-field x-ray microscope at ID06, IOP. Conf. Ser. Mater. Sci. Eng. 580 (2019) 12007, https://doi.org/10.1088/1757-899x/580/1/012007.

[49] C.F. Shih, R.J. Asaro, Elastic-plastic analysis of cracks on bimaterial interfaces: part I—Small scale yielding, J. Appl. Mech. 55 (1988) 299–316, https://doi.org/10.1115/1.3173676.

[50] S. Courtin, C. Gardin, G. Bézine, Hadj ben, H. Hamouda, Advantages of the J-integral approach for calculating stress intensity factors when using the commercial finite element software ABAQUS, Eng. Fract. Mech. 72 (2005) 2174–2185, https://doi.org/10.1016/j.engfracmech.2005.02.003.

[51] T.J. Collins, ImageJ for microscopy, Biotechniques 43 (2007) S25–S30, https://doi.org/10.2144/000112517.

[52] I. Arganda-Carreras, V. Kaynig, C. Rueden, K.W. Eliceiri, J. Schindelin, A. Cardona, et al., Trainable Weka Segmentation: a machine learning tool for microscopy pixel classification, Bioinformatics. 33 (2017) 2424–2426, https://doi.org/10.1093/bioinformatics/btx180.

[53] Fischer-Cripps A.C. Other techniques in nanoindentation. In: Ling FF, editor. Nanoindentation. 3rd ed., New York, NY: Springer New York; 2011, p. 163–80. 10.1007/978-1-4419-9872-9_9.

[54] J.A. Connally, S.B. Brown, Slow crack growth in single-crystal silicon, Science (1979) 256 (1992) 1537–1539, https://doi.org/10.1126/science.256.5063.1537, 1979.

[55] D. Sherman, I. Be'ery, Velocity dependent crack deflection in single crystal silicon, Scr. Mater. 49 (2003) 551–555, https://doi.org/10.1016/S1359-6462(03)00354-3.

[56] D. Sherman, I. Be'ery, From crack deflection to lattice vibrations—Macro to atomistic examination of dynamic cleavage fracture, J. Mech. Phys. Solids. 52 (2004) 1743–1761, https://doi.org/10.1016/j.jmps.2004.02.004.

[57] R.F. Cook, Strength and sharp contact fracture of silicon, J. Mater. Sci. 41 (2006) 841–872, https://doi.org/10.1007/s10853-006-6567-y.

[58] T.B. Britton, A.J. Wilkinson, Measurement of residual elastic strain and lattice rotations with high resolution electron backscatter diffraction, Ultramicroscopy. 111 (2011) 1395–1404, https://doi.org/10.1016/j.ultramic.2011.05.007.

[59] A. Koko, V. Tong, A.J. Wilkinson, T.J. Marrow, An iterative method for reference pattern selection in high-resolution electron backscatter diffraction (HR-EBSD), Ultramicroscopy. 248 (2023), https://doi.org/10.1016/j.ultramic.2023.113705.

[60] C. Maurice, J.H. Driver, R. Fortunier, On solving the orientation gradient dependency of high angular resolution EBSD, Ultramicroscopy. 113 (2012) 171–181, https://doi.org/10.1016/j.ultramic.2011.10.013.

[61] M.A. Hopcroft, W.D. Nix, T.W. Kenny, What is the Young's Modulus of Silicon? Journal of Microelectromechanical Systems 19 (2010) 229–238, https://doi.org/10.1109/JMEMS.2009.2039697.

[62] A.J. Wilkinson, D. Randman, Determination of elastic strain fields and geometrically necessary dislocation distributions near nanoindents using electron back scatter diffraction, Philosophical Magazine 90 (2010) 1159–1177, https://doi.org/10.1080/14786430903304145.

[63] T.B. Britton, J. Jiang, Y. Guo, A. Vilalta-Clemente, D. Wallis, L.N. Hansen, et al., Tutorial: crystal orientations and EBSD — Or which way is up? Mater. Charact. 117 (2016) 113–126, https://doi.org/10.1016/j.matchar.2016.04.008.

[64] K. Shoemake, Euler angle conversion, Heckbert PSBT-GG, editor. Graphics Gems, Elsevier, 1994, pp. 222–229, https://doi.org/10.1016/B978-0-12-336156-1.50030-6.

[65] M. Mostafavi, D.M. Collins, B. Cai, R. Bradley, R.C. Atwood, C. Reinhard, et al., Yield behavior beneath hardness indentations in ductile metals, measured by three-dimensional computed X-ray tomography and digital volume correlation, Acta Mater. 82 (2015) 468–482, https://doi.org/10.1016/j.actamat.2014.08.046.

[66] M.T. Laugier, Palmqvist indentation toughness in WC-Co composites, J. Mater. Sci. Lett. 6 (8) (1987) 897–900, https://doi.org/10.1007/BF01729862, 1987;6.

[67] S. Jiapeng, L. Cheng, J. Han, A. Ma, L. Fang, Nanoindentation induced deformation and pop-in events in a silicon crystal, Molecular Dynamics Simulation and Experiment. Sci Rep 7 (2017) 10282, https://doi.org/10.1038/s41598-017-11130-2.

[68] S. Goel, N. Haque Faisal, X. Luo, J. Yan, A. Agrawal, Nanoindentation of polysilicon and single crystal silicon: molecular dynamics simulation and experimental validation, J. Phys. D. Appl. Phys. 47 (2014) 275304, https://doi.org/10.1088/0022-3727/47/27/275304.

[69] Minor A.M., Lilleodden E.T., Jin M., Stach E.A., Chrzan D.C., Morris J.W. Room temperature dislocation plasticity in silicon. https://doiorg/101080/14786430412331315680 2011;85:323–30. 10.1080/14786430412331315680.

[70] A. Gouldstone, N. Chollacoop, M. Dao, J. Li, A.M. Minor, Y.L. Shen, Indentation across size scales and disciplines: recent developments in experimentation and modeling, Acta Mater. 55 (2007) 4015–4039, https://doi.org/10.1016/J.ACTAMAT.2006.08.044.

[71] A. Koko, In situ characterisation of slip-band behaviour in ferrite under mechanical loading, Proceedings of the Royal Society A: Mathematical, Physical and Engineering Sciences (2025) 481, https://doi.org/10.1098/rspa.2023.0804.

[72] P. Hovington, D. Drouin, R. Gauvin, CASINO: a new monte carlo code in C language for electron beam interaction —Part I: description of the program, Scanning 19 (1997) 1–14, https://doi.org/10.1002/sca.4950190101.

[73] Y.T. Tang, N. D'Souza, B. Roebuck, P. Karamched, C. Panwisawas, D.M Collins, Ultra-high temperature deformation in a single crystal superalloy: mesoscale process simulation and micromechanisms, Acta Mater. 203 (2021) 116468, https://doi.org/10.1016/J.ACTAMAT.2020.11.010.

[74] A.J. Leide, R.I. Todd, D.E.J. Armstrong, Effect of ion irradiation on nanoindentation fracture and deformation in silicon carbide, JOM 73 (2021) 1617–1628, https://doi.org/10.1007/S11837-021-04636-8/FIGURES/8.

[75] R.F. Cook, Y. Gerbig, J. Schoenmaker, S. Stranick, Stress-intensity factor and toughness measurement at the nanoscale using confocal Raman microscopy, in: 12th International Conference on Fracture 2009, ICF-12 5, 2009, pp. 3758–3766.

[76] A.A. Porporati, K. Hosokawa, W. Zhu, G. Pezzotti, Stress dependence of the cathodoluminescence spectrum of N-doped 3C-SiC, J. Appl. Phys. 100 (2006) 093508, https://doi.org/10.1063/1.2363260.

[77] D. Dingley, Progressive steps in the development of electron backscatter diffraction and orientation imaging microscopy, J. Microsc. 213 (2004) 214–224, https://doi.org/10.1111/J.0022-2720.2004.01321.X.

[78] S. Zaefferer, On the formation mechanisms, spatial resolution and intensity of backscatter Kikuchi patterns, Ultramicroscopy. 107 (2007) 254–266, https://doi.org/10.1016/j.ultramic.2006.08.007.

[79] T.C. Isabell, V.P. Dravid, Resolution and sensitivity of electron backscattered diffraction in a cold field emission gun SEM, Ultramicroscopy. 67 (1997) 59–68, https://doi.org/10.1016/S0304-3991(97)00003-X.

[80] D.J. Dingley, V. Randle, Microtexture determination by electron back-scatter diffraction, J. Mater. Sci. 27 (17) (1992) 4545–4566, https://doi.org/10.1007/BF01165988, 1992;27.

[81] B.S. El-Dasher, B.L. Adams, A.D. Rollett, Viewpoint: experimental recovery of geometrically necessary dislocation density in polycrystals, Scr. Mater. 48 (2003) 141–145, https://doi.org/10.1016/S1359-6462(02)00340-8.

[82] A. Bhattacharyya, J.A. Eades, Use of an energy filter to improve the spatial resolution of electron backscatter diffraction, Scanning 31 (2009) 114–121, https://doi.org/10.1002/SCA.20150.

[83] T. Yamamoto, Experimental aspects of electron channeling patterns in scanning electron microscopy. II. Estimation of contrast depth, Physica Status Solidi (a) 44 (1977) 467–476, https://doi.org/10.1002/PSSA.2210440208.

[84] Baba-Kishi KZ, Measurement of crystal parameters on backscatter kikuchi diffraction patterns, Scanning 20 (1998) 117–127, https://doi.org/10.1002/SCA.1998.4950200210.

[85] S.X.X. Ren, E.A.A. Kenik, K.B.B. Alexander, A. Goyal, Exploring spatial resolution in electron back-scattered diffraction experiments via Monte Carlo simulation, Microscopy and Microanalysis 4 (1998) 15–22, https://doi.org/10.1017/S1431927698980011.

[86] R.A. Schwarzer, D.P. Field, B.L. Adams, M. Kumar, A.J. Schwartz, Present State of electron backscatter diffraction and prospective developments, in: A.J. Schwartz, M. Kumar, B.L. Adams, D.P. Field (Eds.), Electron Backscatter Diffraction in Materials Science, Electron Backscatter Diffraction in Materials Science, 53, Springer US, Boston, MA, 2009, pp. 1–20, https://doi.org/10.1007/978-0-387-88136-2_1.

[87] O. Engler, V. Randle, Introduction to Texture Analysis, 2nd ed., CRC Press, 2009 https://doi.org/10.1201/9781420063660.

[88] R.R. Keller, A. Roshko, R.H. Geiss, K.A. Bertness, T.P. Quinn, EBSD measurement of strains in GaAs due to oxidation of buried AlGaAs layers, Microelectron. Eng. 75 (2004) 96–102, https://doi.org/10.1016/j.mee.2003.11.010.

[89] Steinmetz D.R., Zaefferer S. Towards ultrahigh resolution EBSD by low accelerating voltage. https://doiorg/101179/026708309×12506933873828 2013;26:640–5. 10.1179/026708309×12506933873828.

[90] S.F. Bordín, S. Limandri, J.M. Ranalli, G. Castellano, EBSD spatial resolution for detecting sigma phase in steels, Ultramicroscopy. 171 (2016) 177–185, https://doi.org/10.1016/J.ULTRAMIC.2016.09.010.

[91] C. Zhu, M. de Graef, EBSD pattern simulations for an interaction volume containing lattice defects, Ultramicroscopy. 218 (2020) 113088, https://doi.org/10.1016/J.ULTRAMIC.2020.113088.

[92] C.J. Harland, P. Akhter, J.A. Venables, Accurate microcrystallography at high spatial resolution using electron back-scattering patterns in a field emission gun scanning electron microscope, J. Phys. e 14 (1981) 175, https://doi.org/10.1088/0022-3735/14/2/011.

[93] D.J. Dingley, D.P. Field, Electron backscatter diffraction and orientation imaging microscopy, Materials Science and Technology 13 (1997) 69–78, https://doi.org/10.1179/mst.1997.13.1.69.
[94] D. Chen, J.-C. Kuo, W.-T. Wu, Effect of microscopic parameters on EBSD spatial resolution, Ultramicroscopy. 111 (2011) 1488–1494, https://doi.org/10.1016/j.ultramic.2011.06.007.
[95] C.J. Harland, J.H. Klein, P. Akhter, J.A. Venables, Electron back-scattering patterns in a field emission gun scanning electron microscope, in: Proceedings of the 9th International Congress on Electron Microscopy, Toronto 1, 1981, pp. 564–565.
[96] N. Brodusch, H. Demers, R. Gauvin, Imaging with a commercial electron backscatter diffraction (EBSD) camera in a scanning electron microscope: a review, J. ImAging 4 (2018), https://doi.org/10.3390/jimaging4070088.
[97] M. Tanaka, M. Terauchi, K. Tsuda, K. Saitoh, Convergent-beam electron diffraction IV, Jeol 2 (2002).
[98] A. Winkelmann, in: A.J. Schwartz, M. Kumar, B.L. Adams, D.P. Field (Eds.), Dynamical Simulation of Electron Backscatter Diffraction Patterns BT - Electron Backscatter Diffraction in Materials Science, Springer US, Boston, MA, 2009, pp. 21–33, https://doi.org/10.1007/978-0-387-88136-2_2, editors.
[99] W. Wisniewski, C. Rüssel, An experimental viewpoint on the information depth of EBSD, Scanning 38 (2016) 164–171, https://doi.org/10.1002/sca.21251.
[100] C.J. Powell, A. Jablonski, Surface sensitivity of auger-electron spectroscopy and X-ray photoelectron spectroscopy, Journal of Surface Analysis 17 (2011) 170–176, https://doi.org/10.1384/JSA.17.170.
[101] J. PiŇos, Frank L MikmekovÁ, About the information depth of backscattered electron imaging, J. Microsc. 266 (2017) 335–342, https://doi.org/10.1111/JMI.12542.
[102] ISO 18115, 2001/Amd 2:2007 - Surface chemical Analysis — Vocabulary — Amendment 2, 2007.
[103] F.J. Humphreys, Characterisation of fine-scale microstructures by electron backscatter diffraction (EBSD), Scr. Mater. 51 (2004) 771–776, https://doi.org/10.1016/J.SCRIPTAMAT.2004.05.016.
[104] Goldstein J.I., Newbury D.E., Michael J.R., Ritchie N.W.M., Scott J.H.J., Joy D.C. The visibility of features in SEM images. Scanning Electron Microscopy and X-Ray Microanalysis, New York, NY: Springer New York; 2018, p. 123–31. 10.1007/978-1-4939-6676-9_8.
[105] A. Koko, E. Elmukashfi, K. Dragnevski, A.J. Wilkinson, T.J. Marrow, J-integral analysis of the elastic strain fields of ferrite deformation twins using electron backscatter diffraction, Acta Mater. 218 (2021) 117203, https://doi.org/10.1016/j.actamat.2021.117203.
[106] A. Koko, E. Elmukashfi, T.H. Becker, P.S. Karamched, A.J. Wilkinson, T. J. Marrow, In situ characterisation of the strain fields of intragranular slip bands in ferrite by high-resolution electron backscatter diffraction, Acta Mater. 239 (2022) 118284, https://doi.org/10.1016/j.actamat.2022.118284.
[107] T.J. Hardin, T.J. Ruggles, D.P. Koch, S.R. Niezgoda, D.T. Fullwood, E.R. Homer, Analysis of traction-free assumption in high-resolution EBSD measurements, J. Microsc. 260 (2015) 73–85, https://doi.org/10.1111/jmi.12268.
[108] T.H. Becker, M. Mostafavi, R.B. Tait, T.J. Marrow, An approach to calculate the J-integral by digital image correlation displacement field measurement, Fatigue Fract. Eng. Mater. Struct. 35 (2012) 971–984, https://doi.org/10.1111/j.1460-2695.2012.01685.x.
[109] Systèmes® D. ABAQUS. ABAQUS v66 2009. https://classes.engineering.wustl.edu/2009/spring/mase5513/abaqus/docs/v6.6/index.html.
[110] A. Masolin, P.O. Bouchard, R. Martini, M. Bernacki, Thermo-mechanical and fracture properties in single-crystal silicon, J. Mater. Sci. 48 (2013) 979–988, https://doi.org/10.1007/s10853-012-6713-7.
[111] A. Moulins, L. Ma, R. Dugnani, R.J. Zednik, Dynamic crack modeling and analytical stress field analysis in single-crystal silicon using quantitative fractography, Theor. Appl. Fracture Mech. 109 (2020) 102693, https://doi.org/10.1016/J.TAFMEC.2020.102693.
[112] Y. Vertyagina, M. Mostafavi, C. Reinhard, R. Atwood, T.J. Marrow, In situ quantitative three-dimensional characterisation of sub-indentation cracking in polycrystalline alumina, J. Eur. Ceram. Soc. 34 (2014) 3127–3132, https://doi.org/10.1016/J.JEURCERAMSOC.2014.04.002.
[113] Laurie Palasse; Jaroslav Lukeš. In-situ SEM nanoindentation combined with 3D EBSD. 2021.
[114] B. Lawn, R. Wilshaw, Indentation fracture: principles and applications, J. Mater. Sci. 10 (1975) 1049–1081, https://doi.org/10.1007/BF00823224.
[115] G.R. Anstis, P. Chantikul, B.R. Lawn, D.B. Marshall, A critical evaluation of indentation techniques for measuring fracture toughness: I, direct crack measurements, J. Am. Ceramic Soc. 64 (1981) 533–538, https://doi.org/10.1111/j.1151-2916.1981.tb10320.x.
[116] D.B. Marshall, B.R. Lawn, A.G. Evans, Elastic/plastic indentation damage in ceramics: the lateral crack system, J. Am. Ceramic Soc. 65 (1982) 561–566, https://doi.org/10.1111/J.1151-2916.1982.TB10782.X.
[117] B. Lawn, R. Wilshaw, Indentation fracture: principles and applications, J. Mater. Sci. 10 (6) (1975) 1049–1081, https://doi.org/10.1007/BF00823224, 1975;10.
[118] A.G. Evans, E.A. Charles, Fracture toughness determinations by indentation, J. Am. Ceramic Soc. 59 (1976) 371–372, https://doi.org/10.1111/J.1151-2916.1976.TB10991.X.
[119] D.B. Marshall, B.R. Lawn, Residual stress effects in sharp contact cracking, J. Mater. Sci. 14 (1979) 2001–2012, https://doi.org/10.1007/BF00551043, 1979 14:8.
[120] B.R. Lawn, A.G. Evans, D.B. Marshall, Elastic/plastic indentation damage in ceramics: the median/radial crack system, J. Am. Ceramic Soc. 63 (1980) 574–581, https://doi.org/10.1111/j.1151-2916.1980.tb10768.x.
[121] N. Cuadrado, D. Casellas, M. Anglada, E. Jiménez-Piqué, Evaluation of fracture toughness of small volumes by means of cube-corner nanoindentation, Scr. Mater. 66 (2012) 670–673, https://doi.org/10.1016/j.scriptamat.2012.01.033.
[122] R.D. Dukino, Mv. Swain, Comparative measurement of indentation fracture toughness with Berkovich and Vickers indenters, J. Am. Ceramic Soc. 75 (1992) 3299–3304, https://doi.org/10.1111/j.1151-2916.1992.tb04425.x.
[123] G.D. Quinn, R.C. Bradt, On the Vickers indentation fracture toughness test, J. Am. Ceramic Soc. 90 (2007) 673–680, https://doi.org/10.1111/J.1551-2916.2006.01482.X.
[124] R. Morrell BREBLL, Measurement Good Practice Guide No 9, Palmqvist Toughness for Hard and Brittle Materials, Teddington, 2008.
[125] M. Liu, J.Y. Lin, C. Lu, K.A. Tieu, K. Zhou, T. Koseki, Progress in indentation study of materials via both experimental and numerical methods, Crystals. (Basel) 7 (2017) 258, https://doi.org/10.3390/CRYST7100258, 2017;7:258.
[126] M. Tanaka, K. Higashida, H. Nakashima, H. Takagi, M. Fujiwara, Orientation dependence of fracture toughness measured by indentation methods and its relation to surface energy in single crystal silicon, Int. J. Fract. 139 (3) (2006) 383–394, https://doi.org/10.1007/S10704-006-0021-7, 2006139.
[127] J. Qin, Y. Huang, K.C. Hwang, J. Song, G.M. Pharr, The effect of indenter angle on the microindentation hardness, Acta Mater. 55 (2007) 6127–6132, https://doi.org/10.1016/J.ACTAMAT.2007.07.016.
[128] T.B. Britton, H. Liang, F.P.E. Dunne, A.J. Wilkinson, The effect of crystal orientation on the indentation response of commercially pure titanium: experiments and simulations, Proc. Royal Soc. A: Math., Phys. Eng. Sci. 466 (2010) 695–719, https://doi.org/10.1098/RSPA.2009.0455.
[129] F. Ebrahimi, L. Kalwani, Fracture anisotropy in silicon single crystal, Mater. Sci. Eng.: A 268 (1999) 116–126, https://doi.org/10.1016/S0921-5093(99)00077-5.
[130] V.A. Lapitskaya, T.A. Kuznetsova, A v. Khabarava, S.A. Chizhik, S.M. Aizikovich, Ev. Sadyrin, et al., The use of AFM in assessing the crack resistance of silicon wafers of various orientations, Eng. Fract. Mech. 259 (2022) 107926, https://doi.org/10.1016/J.ENGFRACMECH.2021.107926.
[131] P. Zhu, Y. Zhao, S. Agarwal, J. Henry, S.J. Zinkle, Toward accurate evaluation of bulk hardness from nanoindentation testing at low indent depths, Mater. Des. 213 (2022) 110317, https://doi.org/10.1016/J.MATDES.2021.110317.
[132] Z. Li, A. Ghosh, A.S. Kobayashi, R.C. Bradt, Indentation fracture toughness of sintered silicon carbide in the Palmqvist crack regime, J. Am. Ceramic Soc. 72 (1989) 904–911, https://doi.org/10.1111/j.1151-2916.1989.tb06242.x.
[133] G.M. Pharr, E.G. Herbert, Y. Gao, The indentation size effect: a critical examination of experimental observations and mechanistic interpretations, Annu Rev. Mater. Res. 40 (2010) 271–292, https://doi.org/10.1146/annurev-matsci-070909-104456.
[134] E. Broitman, Indentation hardness measurements at macro-, micro-, and nanoscale: a critical overview, Tribol. Lett. 65 (2017) 1–18, https://doi.org/10.1007/S11249-016-0805-5/FIGURES/16.
[135] R. Roy, M. Topping, M.R. Daymond, In-situ assessment of microscale crack tip fields in zirconium, Int. J. Mech. Sci. 264 (2024) 108812, https://doi.org/10.1016/j.ijmecsci.2023.108812.
[136] S. Mohammadi, New Frontiers, in: S. Mohammadi (Ed.), Extended Finite Element Method, Blackwell Publishing Ltd, Oxford, UK, 2008, pp. 189–217, https://doi.org/10.1002/9780470697795.
[137] E. Giner, N. Sukumar, J.E. Tarancón, F.J. Fuenmayor, An Abaqus implementation of the extended finite element method, Eng. Fract. Mech. 76 (2009) 347–368, https://doi.org/10.1016/j.engfracmech.2008.10.015.
[138] A. Karlsson, J. Bäcklund, J-integral at loaded crack surfaces, Int. J. Fract. (1978) 14, https://doi.org/10.1007/BF00116006.
[139] M.C. Walters, G.H. Paulino, R.H. Dodds, Interaction integral procedures for 3-D curved cracks including surface tractions, Eng. Fract. Mech. 72 (2005) 1635–1663, https://doi.org/10.1016/j.engfracmech.2005.01.002.
[140] A. KC, J.H. Kim, Interaction integrals for thermal fracture of functionally graded materials, Eng. Fract. Mech. 75 (2008) 2542–2565, https://doi.org/10.1016/j.engfracmech.2007.07.011.
[141] H. Haftbaradaran, J. Qu, A path-independent integral for fracture of solids under combined electrochemical and mechanical loadings, J. Mech. Phys. Solids. 71 (2014) 1–14, https://doi.org/10.1016/j.jmps.2014.06.007.
[142] C.F. Shih, B. Moran, T. Nakamura, Energy release rate along a three-dimensional crack front in a thermally stressed body, Int. J. Fract. 30 (1986) 79–102, https://doi.org/10.1007/BF00034019.
[143] H. Ming-Yuan, J.W. Hutchinson, Crack deflection at an interface between dissimilar elastic materials, Int. J. Solids. Struct. 25 (1989) 1053–1067, https://doi.org/10.1016/0020-7683(89)90021-8.
[144] H. Yu, L. Wu, L. Guo, Q. He, S. Du, Interaction integral method for the interfacial fracture problems of two nonhomogeneous materials, Mech. Mater. 42 (2010) 435–450, https://doi.org/10.1016/j.mechmat.2010.01.001.
[145] H. Yu, L. Wu, L. Guo, S. Du, Q. He, Investigation of mixed-mode stress intensity factors for nonhomogeneous materials using an interaction integral method, Int. J. Solids. Struct. 46 (2009) 3710–3724, https://doi.org/10.1016/j.ijsolstr.2009.06.019.
[146] J.K. Knowles, E. Sternberg, On a class of conservation laws in linearized and finite elastostatics, Arch. Ration. Mech. Anal. 44 (1972) 187–211, https://doi.org/10.1007/BF00250778.
[147] J.D. Eshelby, The force on an elastic singularity, Philos. Trans. Royal Soc. London Series A, Math. Phys. Sci. 244 (1951) 87–112, https://doi.org/10.1098/rsta.1951.0016.
[148] H. Yu, J. Liu, P. Karamched, A.J. Wilkinson, F. Hofmann, Mapping the full lattice strain tensor of a single dislocation by high angular resolution transmission

Kikuchi diffraction (HR-TKD), Scr. Mater. 164 (2019) 36–41, https://doi.org/10.1016/j.scriptamat.2018.12.039.
[149] M. Lazar, E. Agiasofitou, Eshelbian dislocation mechanics: J-, M-, and L-integrals of straight dislocations, Mech. Res. Commun. 93 (2018) 89–95, https://doi.org/10.1016/J.MECHRESCOM.2017.09.001.
[150] K.P. Baxevanakis, A.E. Giannakopoulos, Finite element analysis of discrete edge dislocations: configurational forces and conserved integrals, Int. J. Solids. Struct. 62 (2015) 52–65, https://doi.org/10.1016/J.IJSOLSTR.2015.01.025.
[151] A. Koko, A. Abdelnour, T.H. Becker, T.James Marrow, Bridging experiments and defects' mechanics: a data- driven toolbox for configurational force analysis, Eng. Comput. (Under Rev.) (2025).
[152] O. Muránsky, L. Balogh, M. Tran, C.J. Hamelin, J.S. Park, M.R. Daymond, On the measurement of dislocations and dislocation structures using EBSD and HRSD techniques, Acta Mater. (2019), https://doi.org/10.1016/J.ACTAMAT.2019.05.036.
[153] J.H. Chang, A.J. Chien, Evaluation of M-integral for anisotropic elastic media with multiple defects, Int. J. Fract. 114 (2002) 267–289, https://doi.org/10.1023/A:1015561313059.
[154] P.S. Karamched, A.J. Wilkinson, High resolution electron back-scatter diffraction analysis of thermally and mechanically induced strains near carbide inclusions in a superalloy, Acta Mater. 59 (2011) 263–272, https://doi.org/10.1016/J.ACTAMAT.2010.09.030.
[155] Y. Guo, C. Zong, T.B. Britton, Development of local plasticity around voids during tensile deformation, Mater. Sci. Eng.: A 814 (2021) 141227, https://doi.org/10.1016/J.MSEA.2021.141227.
[156] J.D. Eshelby, R.E. Peierls, The determination of the elastic field of an ellipsoidal inclusion, and related problems, Proc. R. Soc. Lond. Math. Phys. Sci. 241 (1957) 376–396, https://doi.org/10.1098/rspa.1957.0133.
[157] T. Hui, Y.H. Chen, The M-integral analysis for a nano-inclusion in plane elastic materials under uni-axial or bi-axial loadings, J. Appl. Mech., Trans. ASME 77 (2010) 1–9, https://doi.org/10.1115/1.3176997/469765.
[158] Y. Guo, T.B. Britton, A.J. Wilkinson, Slip band–grain boundary interactions in commercial-purity titanium, Acta Mater. 76 (2014) 1–12, https://doi.org/10.1016/J.ACTAMAT.2014.05.015.
[159] Y. Guo, D.M. Collins, E. Tarleton, F. Hofmann, A.J. Wilkinson, Britton T ben, Dislocation density distribution at slip band-grain boundary intersections, Acta Mater. 182 (2020) 172–183, https://doi.org/10.1016/j.actamat.2019.10.031.
[160] J. Cockle, Notes on the theory of algebraic equations, Mech.' Magazine 55 (1851) 331.